Summer 8-2-2024

INVESTIGATING THE PRODUCTION OF AF96 STEEL ALLOY BY ADDITIVE MANUFACTURING USING DRY METAL ALLOYING

John Paul Osabutey

INVESTIGATING THE PRODUCTION OF AF96 STEEL ALLOY BY ADDITIVE MANUFACTURING USING DRY METAL ALLOYING

by

John Paul Osabutey

A thesis submitted in partial fulfillment of the
requirements for the degree of

M.S. in General Engineering

Montana Tech
2024

Abstract

The design of new alloys specifically for metal additive manufacturing (AM) is an emerging field of research. At present, metal AM primarily utilizes pre-alloyed powders, which are costly and lack flexibility in varying chemical compositions. This study outlines the adaptation of rapid alloy development in laser powder bed fusion (L-PBF) using elemental and ferro-alloyed powder blends. This method enables a more agile and resource-efficient approach to designing and screening new alloys, allowing for the swift generation of alloys with diverse chemical compositions. This thesis investigates the development of AF96 steel alloy through the innovative approach of mixing different elemental powders, utilizing Dry Metal Alloying (DMA) as the primary technique. Dry Metal Alloying uses multiple elemental and ferro-alloyed powders with a known composition mixed in proportion to achieve a desired bulk composition. The study employed a Resonant Acoustic Mixer (LabRAM II) to blend six distinct powder combinations to form the AF96 steel alloy. Notably, AF96 steel alloy has not been extensively explored for use in laser powder bed fusion (L-PBF), despite its potential benefits in enhancing the properties and performance of additively manufactured components. This research underscores the importance of exploring AF96 steel in L-PBF due to its promising applications in producing high-strength, high performance, low cost, and wear-resistant parts. The study meticulously examined the influence of various processing parameters and the resultant linear energy density input on the homogeneity of the manufactured parts. Comprehensive characterization of the powders and deposits was conducted using Scanning Electron Microscopy (SEM), Energy Dispersive Spectroscopy (EDS), X-Ray Fluorescence (XRF), and Arc Spark Optical Emission Spectroscopy (OES). These techniques provided detailed insights into the elemental distribution, and chemical composition of the alloy. Furthermore, the mechanical properties of the DMA deposits were rigorously evaluated to assess their suitability for practical applications. The findings of this research contribute significantly to the understanding of alloy development via elemental and ferro-alloyed powder mixing specifically Dry Metal Alloying and highlight the potential of AF96 steel alloy in advancing the capabilities of metal additive manufacturing.

Keywords: Additive Manufacturing, Dry Metal Alloying, AF96 Steel, Laser Powder Bed Fusion, Elemental Mixing, and Ferro-alloyed Mixing

Dedication

To my Mum and Dad, my brothers and sisters and the Gebrandts for their unconditional love and support. Your belief in me has been a constant source of strength and motivation.

Acknowledgements

I would like to express my deepest gratitude to my advisor, Dr. Nathan Huft, for his exceptional mentorship, unwavering support, and insightful guidance throughout this journey. Your expertise, encouragement, and patience have been instrumental in shaping this thesis and my growth as a researcher. I am profoundly grateful for your commitment to my success and for the countless hours you have dedicated to helping me achieve my academic goals.

I am also deeply appreciative of my committee members, Dr. Peter Lucon, and Dr. Vadiraja Sudhakar, for their invaluable contributions, insights, and encouragement. Your diverse perspectives and expertise have greatly enhanced the quality of this research, and your constructive critiques have guided me to refine and strengthen my work. Thank you for your time, effort, and unwavering support throughout this process.

Finally, I would like to thank Stephen Hanson, Cristina Stefanescu, Jeff Guthrie and Hrudaya Biswal, the entire Montana Tech Advanced Manufacturing Group and Army Research Laboratory (ARL). Your collaboration and intellectual exchanges have been a source of inspiration and motivation. I am grateful for your contributions, whether through stimulating discussions, shared resources, or moral support. Your encouragement has made this journey both enjoyable and fulfilling.

Table of Contents

ABSTRACT .... **II**

DEDICATION .... **III**

ACKNOWLEDGEMENTS .... **IV**

LIST OF TABLES .... **VIII**

LIST OF FIGURES .... **IX**

LIST OF EQUATIONS .... **XII**

GLOSSARY OF ABBREVIATIONS .... **XIII**

1. INTRODUCTION 1

1.1. Research Objective 3

2. BACKGROUND 5

2.1. Manufacturing Processes 5

2.2. Growing Technologies and Trends in Additive Manufacturing (AM) 6

2.2.1. Status of Technology 6

2.2.2. Advantages and Disadvantages of AM 8

2.2.3. Applications of AM 9

2.3. Classification of Materials in AM 10

2.3.1. Metal AM 10

2.4. Powder Bed Fusion Processes 13

2.4.6. Laser Powder Bed Fusion (L-PBF) 14

2.5. L-BPF Process Systems 16

2.5.1. Heat Source (Laser) 16

2.5.2. Laser Powder Bed Fusion Process Parameters 18

2.6. Volumetric Energy Density (VED) 20

2.7. Defects Classification In LPBF 21

2.7.1. Powder-Related Defects 22

2.7.2. Processing-Related Defects 23

2.8. Composition of AF96 24

2.8.1. Impurities in Composition 25

2.8.2. Function of Individual Powders in AF96 Composition 26

2.9. Powder Metallurgy 27

2.9.1. Mechanical Methods 27

2.9.2. Chemical Methods 28

2.9.3. Physical Methods (Atomization) 29

2.10. Mixing Methods for Powders 31

2.11. Dry Metal Alloying 34

2.12. Phase Transformation of Low Alloy Steels Welds 34

3. MATERIALS AND METHODS 40

3.1. DMA Constituent Powder 40

3.2. Particle Size Distribution 40

3.3. Powder Morphology 41

3.4. DMA Powder Composition 41

3.5. AF96 DMA Mixing 42

3.5.1. Phase One 42

3.5.2. Mixing Parameters 43

3.6. DMA AF96 Powder Characterization 44

3.6.1. X-Ray Fluorescence Spectrometry (XRF) 44

3.7. Preliminary Printing Investigations 45

3.7.1. ONE Click Metal Printer 45

3.7.2. Phase One Printing Parameters 46

3.7.3. Arc-Spark OES 47

3.7.4. Sample Preparation 48

3.7.5. SEM-EDS Line Scans 48

3.8. Mechanical Testing 49

3.9. AF96 DMA Mixing and Printing Parameters for Phase Two 49

4. RESULTS AND DISCUSSION 51

4.1. Particle Size Distribution and Morphology Analysis 51

4.2. PSD and Morphology of DMA AF96 Alloy 55

4.3. X-Ray Fluorescence Spectrometry (XRF) Analysis 56

4.4. Preliminary Printing Results 56

4.5. ARC Spark Spectrometry Analysis 57

4.6. SEM Analysis for Phase One 60

4.6.1. SEM Analyses for Phase Two 62

4.6.2. Discontinuities and Void Formation in Melt Pool 64

4.6.3. SEM Micrographs Showing Less Discontinuities 65

4.6.4. Arc Spark Spectrometry Analysis for Phase 2 Experiments 67

4.6.5. SEM-EDS Lines Scan Analysis 67

4.6.6. Comparison of %RSD of DMA AF96 Deposits to Industrially Cast Alloy 69

4.7. Rockwell Hardness Test Results 69

5. CONCLUSION 71

6. RECOMMENDATION 72

6.1. DMA Powder Composition 72

6.2. L-PBF Deposits 72

7. REFERENCES CITED 73

8. APPENDIX A 83

List of Tables

Table I: Applications, Materials, Benefits, and Drawbacks of Additive Manufacturing Methods [38] 13
Table II: Process Properties of Some Powder Bed AM Technologies [40] 14
Table III: AF96 Composition by Weight[49] 25
Table IV:Chemical Composition of H13, 420 Stainless Steel and 4340 42
Table V: PSD Results for Constituent Powders 52
Table VI: XRF Results for DMA AF96 Composition One and Two 56
Table VII: Arc Spark Spectrometry Results of Phase 1 AF96 Deposits 58
Table VIII: Arc Spark Spectrometry Results of Phase 2 AF96 deposits 67
Table IX: %RSD Values for DMA Deposits and Industrial Cast Alloy 69
Table X: Composition Calculator for Composition One 83
Table XI: Composition Calculator for Composition Two 83

List of Figures

Figure 1: Schematic Diagram Illustrating Process of Pre-alloyed and DMA Powder (Adapted from [16])....3

Figure 2: Additive Manufacturing Process Categories According to ASTM/ISO 52900:2015 [31] 7

Figure 3: Schematic Diagram of a Laser Powder Bed Fusion Process [39]....15

Figure 4: Power Density Distribution with a Power Source of 450 W and 2mm Radius [42] 17

Figure 5: L-PBF Detailed Printing Parameters [31] 19

Figure 6: Defect Morphologies in L-BPF Metal AM [12] 24

Figure 7: A Schematic Diagram of Water Atomization Process [52] 31

Figure 8: “Schematic Diagram of Continuous Cooling Transformation Diagram Showing the Development of Weld Metal Microstructure in Low Alloy Steels. (I) inclusion formation, (II) solidification of liquid to ferrite, (III) fully austenitic structure, (IV) [61] 38

Figure 9: Micrograph Showing the Microstructures for a Low Alloy Steel Weld Metal: A, grain boundary ferrite; B, polygonal ferrite; C, Widmansatten ferrite; D, acicular ferrite; E, upper bainite; F, lower bainite [62]....39

Figure 10: 8-fluid-ounce Mixing Fluid Vessel Containing Constituent Metal Powders Before Mixing....43

Figure 11: Mixing Vessel for DMA AF96 in RAM 44

Figure 12: (a) Sampling Lid Showing Five Different Sampling Positions, (b) Sampling Thief 45

Figure 13: (a) Commercial OneClick MPRINT Printer, (b) MPURE System 46

Figure 14: Schematic of Printing Parameters for Preliminary Investigation....................47

Figure 15: Sectioned and Hot Mounted AF96 Samples Showing X,Y, and Z Planes.......49

Figure 16: Build Strategy for Phase 2 Experiments..50

Figure 17: PSD Analysis for AF96 Constituent Powders..51

Figure 18: SEM Micrograph for Irregular Iron Powder at 100X, 300X, and 800X..........52

Figure 19: SEM Micrographs of H13 Powder at 100 X, 300X and 800X........................53

Figure 20: SEM Micrographs of 420 Stainless Steel Powder at 100 X, 300X and 800X .53

Figure 21: SEM Micrographs of Ferronickel Powder at 100 X, 300X and 800X............54

Figure 22: SEM Micrographs of Ferromolybdenum Powder at 100 X, 300X and 800X..54

Figure 23: SEM Micrographs of 4340 Steel Powder at 100 X, 300X and 800X 55

Figure 24: PSD (a) and Morphology (b) of DMA AF96 Alloy.......................................55

Figure 25: Printed Cubes of AF96 Deposits Showing Printing Defects...........................57

Figure 26: Arc Spark Analysis of Carbon Wt.% Vs. Energy Density..............................59

Figure 27: Arc Spark Analysis of Molybdenum Wt.% Vs. Energy Density 60

Figure 28: SEM Micrographs of the Printed Deposits with Increasing Linear Energy Density Showing Heterogeneous Composition. Arrows Pointing to Heterogeneous Regions 62

Figure 29: SEM Micrographs of Phase 2 Deposits Showing Improved Homogeneity. Arrows Pointing to Heterogenous Regions..63

Figure 30: SEM Micrographs Showing Discontinuities in Phase 1 Deposits 64

Figure 31: Wide Field SEM Micrographs Showing Less Discontinuities at Slower Travel Speeds 66

Figure 32: AF96 Constituent %RSD Vs. Energy Density...68

Figure 33: Relationship between Hardness and Linear Energy Density 70

List of Equations

Equation (1) 20

Equation (2) 20

Equation (3) 20

Glossary of Abbreviations

Term	Definition
AM	Additive Manufacturing
ASMT	American Society for Testing and Materials
BJT	Binder Jetting
CAD	Computer Aided Design
CAGR	Compound Annual Growth Rate
CCD	Charged Coupled Device
DED	Direct Energy Deposition
DMA	Dry Metal Alloying
DMLM	Directed Metal Laser Melting
DI	Deionized
EBM	Electron Beam Melting
EDS	Energy Dispersive X-ray Spectrometry
FDM	Fused Deposition Modeling
IIW	International Institute of Welding
ISO	International Organization of Standardization
LabRAM	Laboratory Resonant Acoustic Mixer
LOF	Lack of Fusion
L-PBF	Laser Powder Bed Fusion
MJ	Material Jet
NMI’s	Non-Metallic Inclusions

OES	Optical Omission Spectrometry
PSD	Particle Size Distribution
SEM	Scanning Electron Microscope
SLA	Stereolithography
SLM	Selective Laser Melting
SLS	Selective Laser Sintering
VED	Volumetric Energy Density
2D	Two-Dimensional
3D	Three-Dimensional

1. Introduction

Laser powder bed fusion (L-PBF) represents an additive manufacturing (AM) technique wherein the metal powder is deposited onto a substrate and selectively melted with a laser, building layer by layer to form a three-dimensional object [1-3]. In recent years, metal additive manufacturing has garnered escalating industrial attention for producing functional components. Parts generated through additive manufacturing exhibit innovative shapes, complex features, and lightweight structures that are impossible to produce with conventional processes such as formative and subtractive methods [4].

In spite of its considerable advantages in comparison to traditional subtractive and formative manufacturing methods, the utilization of parts fabricated through L-PBF in mission-critical sectors such as aerospace & energy generation industries is presently constrained by inherent process deficiencies, such as lack of fusion porosity, cracking, and shape distortion [5-7]. Once the feedstock material is established, issues pertaining to part quality may be ascribed to AM process parameter settings, usually determined through a trial-and-error method.

Establishing a connection between AM process and part characteristics ensures desirable part quality and fosters widespread adoption of technology. Upon establishing this correlation, in-process sensing, and real-time control of AM process parameters can be implemented to minimize variations throughout the AM build process, guaranteeing the quality of the resulting product and facilitating production efficiency [8].

The formation of flaws and defects in Laser Powder Bed Fusion (L-PBF) parts during melt pool and part-level thermal interaction is influenced by several factors. These factors are:

- Properties of the feedstock powder material, such as the distribution of powder particles, thermal conductivity, presence of gas entrapment, and contaminants
- Processing parameters, including laser power, hatch spacing, scan speed, and pattern
- Quantity, shape, and positioning of parts on the build plate
- Part's characteristics, including its shape, orientation, and the support structure design
- Process faults stemming from anomalies associated with the machinery [6][9-12]

Powders are complex materials, as such, understanding powder materials is a challenge because they are an assembly of multiple individual particles. Each constituent particle manifests distinct properties, collectively influencing the characteristics of the powder bulk. Consequently, the properties of the bulk powder may vary significantly depending on factors such as particle arrangement or packing and the number of particles that make up the bulk [13-15].

Novel metal alloy powders such as the AF96 steel alloy are being developed for Powder Bed Fusion (PBF) by the Montana Tech Advanced Manufacturing group (MTAM). This specific alloy is designed to unlock the unique capabilities of PBF technologies while meeting the rigorous demands of critical industries such as medical, aerospace, nuclear, military, and oil and gas. The AF96 steel alloy, for instance, offers enhanced strength and toughness, and high performance even at temperatures of -40° F to -65° F.

This study addresses the growing need to develop cost-effective, flexible, homogeneous, and efficient alloy production methods using the Dry Metal Alloying (DMA) technique (Figure 1). The flow chart in Figure 1 illustrates how pre-alloys after production have fixed composition, whereas alloys produced via DMA have adjustable compositions with several constituent powders. The study focuses on producing DMA AF96 steel alloy with several constituent alloys as the bulk feedstock (printable on a One Click MPRINT printer). Dry Metal Alloying from elemental and ferro-alloy powders offers extensive flexibility in adjusting compositions for any alloy, especially those with powders such as vanadium that are difficult to procure.

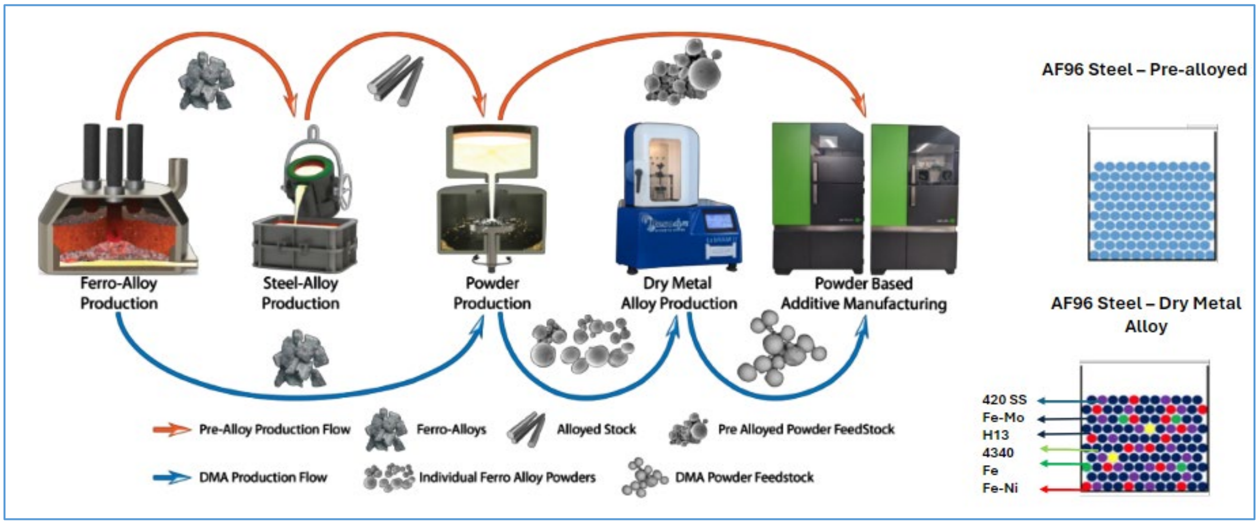

Figure 1: Schematic Diagram Illustrating Process of Pre-alloyed and DMA Powder (Adapted from [16])

1.1. Research Objective

Conventional feedstock powders for AM processes are pre-alloyed powder feedstock. Nevertheless, considering the flexibilities and distinct advantages offered by AM methods, there arises a need for an integrated framework encompassing methodologies and phenomena to facilitate the development of new alloys with innovative properties. The use of pre-alloyed powders not only constraints the judicious customization of compositions, thereby limiting the potential to create unconventional alloy composition and properties, but has also been demonstrated to be economically nonviable and costly [17][18].

It is crucial to comprehend the reasons why DMA powder is not commonly utilized, as well as the potential advantages it may offer for additive manufacturing (AM). In this thesis, Dry Metal Alloying (DMA) AF96 mixed powders are anticipated to exhibit homogeneity throughout the bulk powder mixture and printable on the commercial One Click MPRINT printer. The homogeneity of the DMA AF96 deposits should be comparable to that of an industrially cast alloy and should be maintained throughout the deposition process of the DMA powder. To ensure the replication of the quality and characteristics of the DMA powders within their respective deposits, the mixing and powder deposition processes were conducted in two phases which is essential to achieve consistent results.

2. Background

2.1. Manufacturing Processes

Manufacturing processes are typically divided into three categories, with additive manufacturing being one of the main categories. The other two categories are subtractive processes and forming processes [19][20].

Forming process includes forging, casting, molding, or bending which is used to shape materials into specific shapes and geometries. Forming processes involve the remodeling of raw materials into desired structures or shapes by applying mechanical forces or heat. In the manufacturing process, the raw materials are completely displaced and deformed into desired shapes and structures hence no material is removed contrary to subtractive manufacturing or processes [21].

Subtractive manufacturing encompasses various methods for creating a finished or intermediate stage product by removal of material. Some processes under this category consist of drilling, turning, milling, boring, broaching, and grinding [22].

Contrary to subtractive manufacturing and formative manufacturing methodologies, additive manufacturing (AM) consists of technologies that allow the creation of three-dimensional (3D) objects by adding materials layer by layer [23]. The additive nature is desirable for manufacturing parts with complex geometries and a variety of materials including metallic, ceramic, and polymeric [24].

2.2. Growing Technologies and Trends in Additive Manufacturing (AM)

2.2.1. Status of Technology

AM has existed since the 1990's, but only lately has this technology risen in popularity and captured the interest of both technology experts and the public. Since the expiration of the last major patent for fused deposition modeling (FDM) in 2009, FDM printers can now be manufactured without violating intellectual property rights. This development has sparked renewed interest and investment in additive manufacturing technologies. Although the AM industry is still in its preliminary stages, ongoing technological advancements, and exploration of novel applications for the technology are in progress. It will require several more years before AM can genuinely revolutionize manufacturing and other industries significantly [25].

As stated in a 2014 report by [25], AM generated a worldwide revenue of $3.07 billion in 2013. These revenues are anticipated to multiply in coming years to about $21 billion. These figures portray that the AM industry is expanding at a rapid rate [25].

In 2021, the global additive manufacturing market reached a value of $13.84 billion. Projections indicate a robust expansion with a 20.8% compound annual growth rate (CAGR) between 2022 and 2030. Notably, 2.2 million 3D printers were shipped worldwide in 2021, a figure expected to surge to 21.5 million units by 2030. The market's upward trajectory is attributed to heightened demands for prototyping across diverse sectors like healthcare, automotive, and aerospace and defense. Additionally, the market's growth is fueled by intensive research and development efforts in 3D printing technologies [26].

In an American Society for Testing and Materials (ASTM) standard in 2009, additive manufacturing was defined as "a process of joining materials to make objects from 3D model data, usually layer upon layer, as opposed to subtractive manufacturing methodologies"[27]. AM processes are categorized into two main categories: (1) fusion-based methods and (2) non-fusion-based methods which are further divided into seven broad subclasses by the ISO/ ASTM 52900: 2015 standard. Figure 2 shows the seven broad subclasses of AM processes. Under fusion-based methods, are directed energy deposition (DED), laser powder bed fusion (L-PBF), electron beam melting (EBM). Non-fusion-based methods are sub-classified as extrusion, binder jet, material jet, and sheet lamination [27-30].

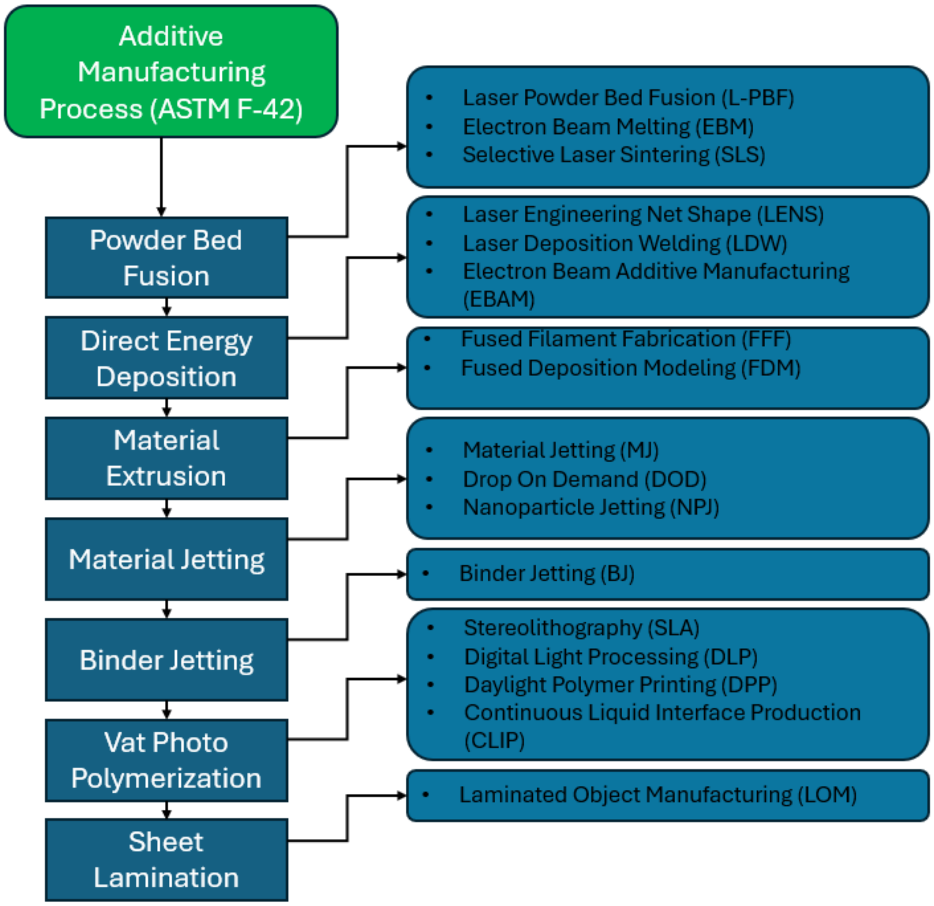

Figure 2: Additive Manufacturing Process Categories According to ASTM/ISO 52900:2015 [31]

2.2.2. Advantages and Disadvantages of AM

In contrast to conventional manufacturing processes, AM processes have the following advantages:

Part Flexibility: AM provides opportunities to essentially eliminate numerous subtractive and formative manufacturing methods such as forging, machining, coating, and joining processes by printing complete parts in one print. A metal acetabular cup, used in hip replacement surgeries, is an example of AM product developed using a laser powder bed fusion metal printer with porous surface built into the layers. This product development has helped over 440,000 people in the United States alone. Its production is categorized as Mass Complexity where parts exhibit complex geometries without customization features [32].

Material Efficiency: Raw materials are used effectively in AM to build parts layer by layer. In contrast, conventional subtractive manufacturing processes remove materials that lead to waste generation. The used powder materials in AM processes are mostly recycled with minimum processing.

Production Flexibility: Additive manufacturing stands out for its cost-effectiveness in small batch production, as it eliminates the need for expensive part-specific setups. The quality of the part relies on the process itself rather than operator skills, enabling easy synchronization with customer demand. Furthermore, complex parts are crafted as single pieces, reducing challenges related to line balancing and production holdups.

Resource Efficiency: In contrast to traditional manufacturing processes that require auxiliary resources like jigs, fixtures, cutting tools, and coolants alongside the main machine tool, AM operates without these additional requirements. As a result, small manufacturers can produce parts that are close to customers' demand thereby fostering improved supply chain dynamics.

The following are the disadvantages of AM processes:

Capital Equipment: The investment required for AM equipment is considerable, ranging from entry-level 3D printers at around $200 to high-end models costing hundreds of thousands of dollars, excluding accessories, resin, or other operational materials.

Size Limitations: AM processes, using liquid polymers, powder, or wire feedstock, face challenges in producing large-sized objects due to material strength limitations. Extended build times further contribute to the impracticality of creating sizable items.

Discontinuities: Parts manufactured through AM processes often exhibit rough and ribbed surface finishes attributed to the stacking of plastic beads or large-sized powder particles. This mostly results in an unfinished appearance.

Researchers are actively addressing these challenges to enhance the capability of AM processes. While it is unlikely that AM will replace traditional manufacturing entirely, it is reasonable to anticipate its increasing role as a complementary technology in the manufacturing landscape [33].

2.2.3. Applications of AM

AM techniques have developed significantly over the years offering enormous industrial applications. AM is specifically desirable for manufacturing parts with intricate geometries. Listed below are some popular applications of AM:

1. Parts manufacturing for aerospace and automotive sectors
2. Mold making and tooling
3. Developing personalized bio-implants (Ti-6AI-4V) utilizing EBM and L-PBF processes.

4. Prototyping for demonstration purposes.
5. Manufacturing structural components through SLS and EBM techniques [34-35].

2.3. Classification of Materials in AM

The standardization of Additive Manufacturing (AM) processes is a relevant step in the progression of metals AM and remains an ongoing process. In 2009, the inception of the American Society for Testing and Materials (ASTM) F42 Committee on AM Technologies was aimed at steering the formulation of international standards in AM. One of such milestones was the approval, in 2012, of the ASMT F2924 Specification for AM Titanium-6 Aluminium-4 Vanadium with Powder Bed Fusion. Additionally, other standardizations, such as ASTM F2792 (establishing standardized AM terminology in 2009) and ASTM F2915 (defining the AM File Format in 2011), were created to further support the advancement of AM.

The standardization of file formats into the Additive Manufacturing File (AMF) format has enabled the seamless transfer of designs across diverse hardware and software systems. This development was engineered to support comprehensive features like full-color-multi-material geometries, including microstructure and material gradients [22]. Materials used in AM applications are classified as metals, polymers, ceramics, biomaterials, and smart materials in the modern manufacturing sector.

2.3.1. Metal AM

Metallic 3D printing plays a crucial role in manufacturing, using a variety of energy sources and materials in modern additive manufacturing advancements. Primarily, metallic 3D printing employs four methods namely, Laser Powder Bed Fusion (L-PBF), Direct Energy Deposition (DED), Binder Jetting, and Laminated Object Manufacturing (LOM). Other techniques such as cold spraying, friction stir welding and diode-based processes are also used for printing metals [36]. Each method utilizes distinct forms of feedstock. In Powder Bed Fusion metallic powder beds are melted using lasers to craft the desired structure. L-PBF and EBM process alloys and pure metals like iron, copper, and gold.

DED employs either powder flow or metal wire as feedstock. Binder Jetting utilizes feedstock in powder bed form, binding it with injected liquid binder. LOM uses metallic sheets as feedstock [37].

Various metallic materials, including stainless and tool steels, certain aluminum and titanium alloys and nickel-based alloys, can be fabricated through L-PBF-based AM processes. L-PBF technologies excel in crafting components with intricate designs, a precision of plus or minus 0.02mm, and commendable mechanical properties. However, these technologies are mainly used for small parts because they are slow (up to 105cm^3/h with four lasers). Research is underway to explore alternative laser types like femtosecond lasers, known primarily for handling alloys and metals with substantial melting temperatures (> 3000°C) and high thermal conductivity (>100W/mK), such as tungsten, rhenium, and select ceramics.

Optimized for AM, titanium and its alloys, steel alloys, a handful of aluminum alloys, nickel alloys, cobalt based, and magnesium alloys have undergone refinement. Titanium and its alloys, notably, serve as high-performance materials widely deployed across diverse industries. Despite their high machining expenses and prolonged production timelines within conventional manufacturing methods, AM presents significant economic advantages by fabricating complex structures at reduced cost and minimal waste. Ti [45] and Ti6AI4V [46] have undergone comprehensive studies and are presently integrated into commercial applications within aerospace and biomedical domains.

AM usually incorporates steels like austenitic stainless steel, maraging steels, precipitation hardenable stainless steel, and tool steels. These alloys cater to general applications and conditions requiring heightened strength and hardness, such as tooling or molding purposes. Austenitic steels and precipitation hardenable stainless steel exhibit particular sensitivity to AM parameters.

The utilization of Al alloys in AM remains limited due to multiple factors. In contrast to Ti alloys, Al alloys are simpler to machine and come at a lower cost. Consequently, there has been less commercial interest in using them for AM. Additionally, certain high-performance Al alloys pose challenges in welding (due to volatility of elements like Zn), while Aluminum's high reflectivity to laser wavelengths commonly used in AM presents another challenge. Furthermore, the low viscosity of molten aluminum restricts a sizeable melting pool, prompting the preference for PBF over DED manufacturing. Nonetheless, Al's high thermal conductivity curbs internal stresses and permits swifter AM processes. Presently, the most prevalent alloys in use are AlSi10 Mg and AlSi12 [38].

Table I presents an outline of materials, applications, advantages and disadvantages and resolution range of some additive manufacturing methods.

Table I: Applications, Materials, Benefits, and Drawbacks of Additive Manufacturing Methods [38]

Methods	Materials	Application	Advantages	Disadvantages
Fused deposition modelling	Filaments of thermoplastic and fibre reinforced polymers	Rapid prototyping, toys and advanced composite parts	High speed, simplicity, and low cost	Poor mechanical properties, limited materials and layer-by-layer finish
Powder bed fusion	Limited polymers and ceramics, compacted fine powders, metals and alloys	Biomedical, aerospace, light weight structures, electronics, and heat exchanger	Fine resolution and high quality	Increased porosity in binder method, expensive and slow printing
Laminated object manufacturing	Metal rolls, ceramics, paper, and polymer composites	Smart structures, electronics, foundry industries and paper manufacturing	Less manufacturing and tooling time, low cost, wide range of materials	Poor surface finish and dimensional accuracy and limitation in producing complex shapes
Direct energy deposition	Ceramics, polymers, metals, and alloys in a form of powder or wire	Biomedical, repair, cladding, retrofitting and aerospace	Decreased manufacturing cost and time, unique mechanical properties, precise composition control, excellent for repair and retrofitting	Poor accuracy and surface finish, necessity for dense support structure, constraint in printing complex parts with fine details

2.4. Powder Bed Fusion Processes

Powder Bed Fusion is a state-of the-art manufacturing technology that can be used to produce parts from 3D computer aided design (CAD) model by adding materials layer by layer. This technology utilizes either electron beam or laser as a source of energy for irradiation, melting and fusion of the powder material. The powder bed fusion technique encompasses L-PBF, Direct Metal Laser Melting (DMLM), and Electron Beam Melting (EBM). Table II below shows some powder bed techniques and their typical properties [39-40].

An inert gas such as nitrogen or argon is provided to the powder bed chamber to ensure the molten metal is shielded. A laser or electron beam is applied to scan the powder layer by layer. The energy source specifically tracks and melts the powder material in accordance with the digital part model. After a layer is scanned the piston for the building chamber drops down and the piston for the powder chamber moves up to a specific powder layer thickness to be spread by a coater or roller. This procedure is replicated until the part is finally completed [41].

Table II: Process Properties of Some Powder Bed AM Technologies [40]

Process	**Energy Source**	**Materials**	**Particle size range (µm)**	**Layer thickness (µm)**	**Pre-heating**
EBM	Electron beam	Metals	50-150	50-100	Yes (electron beam,700-1100 °C)
SLS	Laser	Polymers	20-80	100-150	Yes (180-380 °C)
BJT	Furnace heating	Metals, polymers, ceramics	< 25	50-100	No

2.4.6. Laser Powder Bed Fusion (L-PBF)

Figure 3 displays the schematic representation of a laser powder bed fusion AM system. The LBPF systems are structured with two key components: powder delivery system and energy delivery system. The powder delivery system comprises of a piston responsible for powder supply, coater to produce the powder layer, and piston for retaining the manufactured part. The energy delivery system consists of a laser, often a single-mode continuous-wave Ytterbium fiber laser operating at a wavelength of 1075nm.

As part of the energy delivery system, a scanner system is equipped with optics that facilitate the precise delivery of a focused spot to all areas of the build platform. To shield the part from oxygen exposure and eliminate any generated "spatter" and metal fumes resulting from the laser's path, a stream of gas (typically nitrogen or argon) flows over the powder bed.

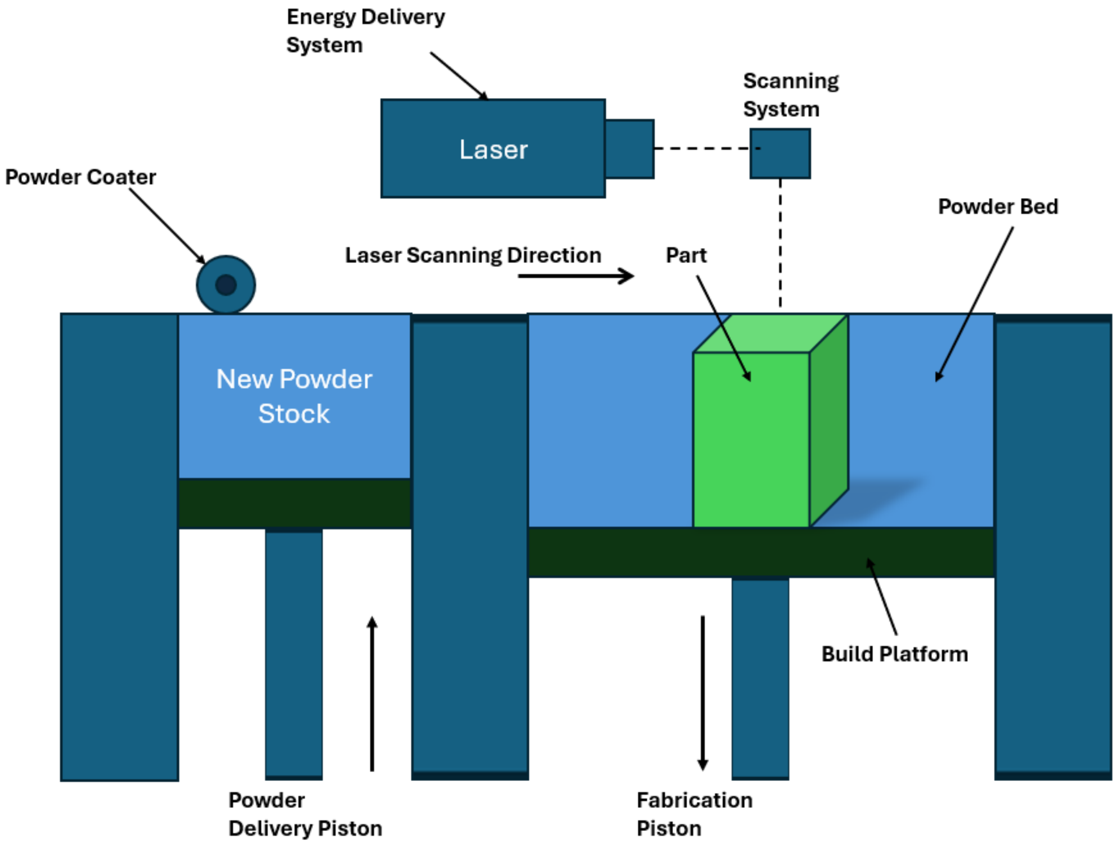

Figure 3: Schematic Diagram of a Laser Powder Bed Fusion Process [39]

While manufacturing, the laser implements a scanning or exposure strategy. The attributes of these strategies linked with the path of the laser are defined by the orientation, length, and hatch spacing of adjacent scan vectors. These scanning approaches impact the characteristics of the manufactured component, such as density, residual stress, and mechanical properties. Residual stress stands out as a crucial material property necessitating optimization for components created through laser-based additive manufacturing.

A component can be manufactured within acceptable tolerances, but the introduction of distortions due to residual stress upon removal from the build plate pushes the component beyond those tolerances. Residual stresses can result in surface distortions that could harm the coating apparatus or impede its motion and even lead to failures in the connections between a component and its support structure [39].

2.5. L-BPF Process Systems

The main components of a typical L-PBF system are laser, scanning systems, powder delivery system, powder deposition system, build platform, powder removal, gas supply, and filtration systems [27].

2.5.1. Heat Source (Laser)

In AM, energy absorption by feedstock materials impacts various aspects, including temperature patterns, deposition shape, solidification, microstructure, and the properties of the final product. The amount of energy absorbed is contingent on the attributes of the heat source. In the case of lasers, electron beams, and plasma arcs, the size and power density distribution play pivotal roles. Frequently, these heat sources exhibit power density distributions that conform to axisymmetric Gaussian profiles.

In Figure 4, the power density is shown as a function of the horizontal position relative to the heat source's axis. The power density distribution can exhibit uniformity depending on the characteristics of the heat source itself. As the distribution factor increases, the energy becomes more concentrated, resulting in elevated peak temperatures directly beneath the heat source. Consequently, the power density distribution serves as a descriptor of the heat source's nature and holds significant importance in the precise fabrication of high-quality AM components[42].

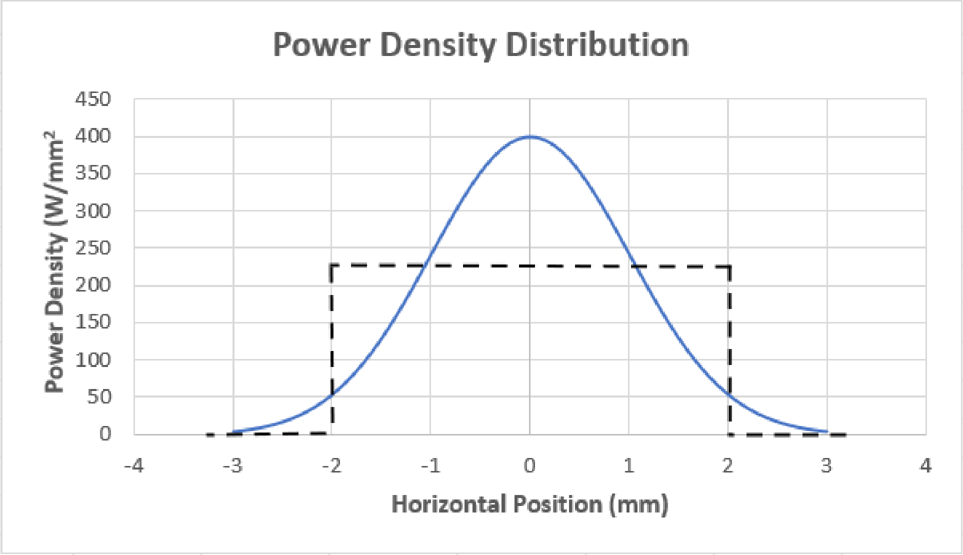

Figure 4: Power Density Distribution with a Power Source of 450 W and 2mm Radius [42]

Methods commonly employed for assessing the energy distribution of laser, electron beam, and arc heat sources are available. Laser beams, characterized by their coherent photon emission, can be measured through solid state Charged Coupled Device (CCD) detectors. However, in the context of AM, the intensity of the laser beam can lead to saturation or damage of the detector, necessitating measures to restrict beam intensity.

To address this issue, a rotating wire mechanism has been utilized for CO_2 laser beams. This approach encompasses spinning a fine wire through the laser beam and gauging the intensity of the reflected laser beam. This technique offers an estimation of the power density distribution of the beam. Recent advancements have presented alternative tools employing a swiftly spinning tube equipped with a small pinhole and mirror. This setup directs a laser beam towards a CCD detector. This innovative method effectively maps the power density of both CO_2 and solid-state lasers, offering a comprehensive insight into their focused beams.

Furthermore, through sampling the beam at diverse points along its propagation axis, it becomes possible to measure the beam's divergence and its minimum spot size. This procedure facilitates a comprehensive characterization of the laser beam, adhering to standardized protocols. The minimum spot sizes utilized in AM are contingent upon the specific process. Powder bed techniques commonly use beam diameters ranging from 50 to 100μm for fine resolution [42-43].

The relationship between metal powder particles and laser radiation in L-BPF is intricate and involves several physical processes. These include chemical reactions and phase transformation, heat transfer, and the intricate fluid flow within the melt pool due to variations in surface tension gradient. Additionally, the absorption and scattering of laser radiation further contributes to this complex interplay of phenomena [43].

2.5.2. Laser Powder Bed Fusion Process Parameters

The L-PBF process involves several physical phenomena. These include laser absorption and reflection, heat transfers, fluid dynamics, vaporization, material emission, and chemical reactions. Phase transitions of powder to liquid and solidification happen simultaneously during this process. Grasping these physical processes is crucial for producing flawless components and selecting optimal L-PBF process parameters.

Common defects in the L-PBF process stem from inadequate heating or excessive heating during melting, specifically impacting overhang structures and unevenly melting parts. To enhance the quality and mechanical properties of printed parts, closely monitoring of printing parameters throughout L-PBF is paramount. Several L-PBF printing parameters influence component buildup in the final phase thereby impacting the relative density. Figure 5 shows the details of various process parameters in the L-PBF process.

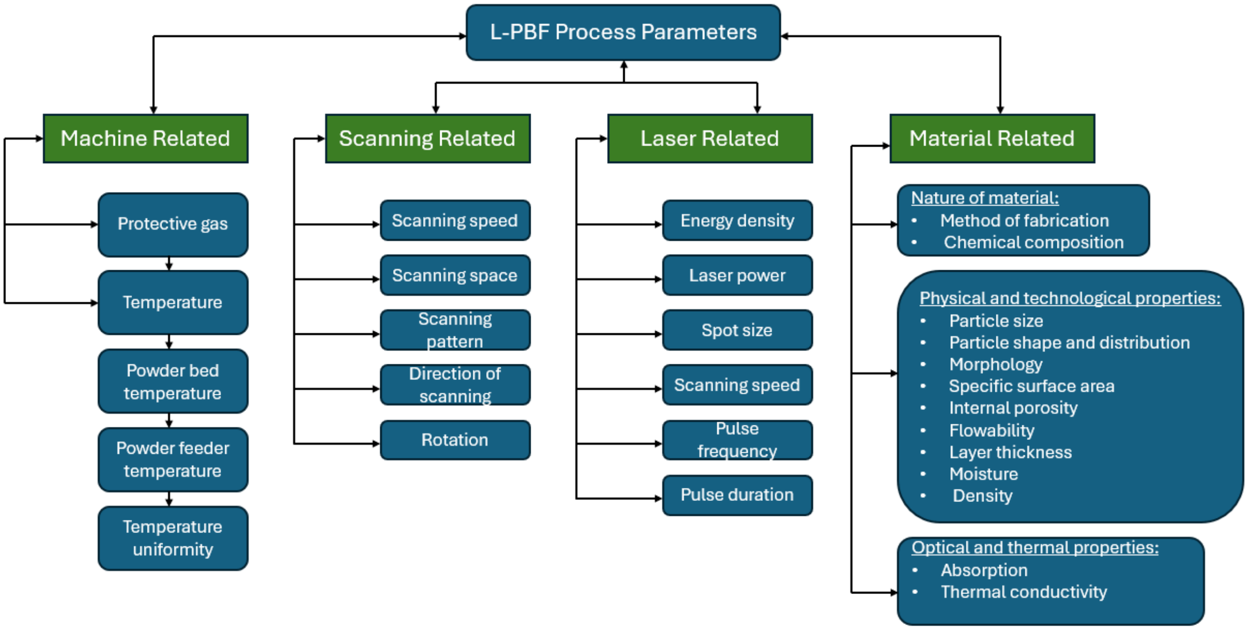

Figure 5: L-PBF Detailed Printing Parameters [31]

Adjusting parameters based on material properties results in decreased residual stress, minimized distortion, and superior printed quality. Effective control of printing parameters is the ultimate approach to achieving desired geometries, mechanical properties, and microstructures. While all aspects of the L-PBF process respond to each printing parameter, it becomes challenging to ascertain the precise level of parameter influence. Nonetheless, the volumetric energy density equations modulate the parameter's range of significance rather than pinpoint values.

2.6. Volumetric Energy Density (VED)

Volumetric Energy Density is a vital manufacturing characteristic concerning the fusion of powder materials. VED reflects the energy from the laser beam transferred to a volumetric quantity of powder material. VED maintains a connection with multiple pertinent laser and scan parameters. Furthermore, there are four individually controlled parameters that VED is made up of:

1. Laser power (W): the energy concentration of the laser beam
2. Scanning speed (mm/s): the velocity at which the laser beam traverses
3. Hatch distance/spacing (mm): the gap present between two adjacent scan paths.
4. Layer thickness (mm): the depth of a single layer, equivalent to an incremental amount of the powder bed [31][44-45].

It is noteworthy that even when the energy density value remains constant, applying different parameters within the L-BPF process leads to varied material properties. Moreover, the energy density value is not the same across materials and surpassing a material's particular energy range results in an expanded and deeper melt pool. VED is denoted as E_v and calculated using the following equations.

$$\boldsymbol{E}_{\mathrm{L}} = \frac{P}{v} \qquad \textbf{(1)}$$

$$\boldsymbol{E}_{\mathrm{A}} = \frac{P}{v \times d} \qquad \textbf{(2)}$$

$$\boldsymbol{E}_{\mathrm{V}} = \frac{P}{v \times d \times t} \qquad \textbf{(3)}$$

P represents output laser power (W), v represents scan speed (mm/s), d represents scan spacing (µm), and t stands for layer height (µm) of the powder. Equation (1) illustrates the formular for linear energy density, E_L (J/mm), and equation (2) is the formula for areal energy density, E_A (J/mm^2). Among these equations, equation 3, which defines VED (volumetric energy density), is the one most frequently cited in literature [44][46].

Alternative research utilizes the laser beam diameter (mm) in place of the hatch distance. Meanwhile, it is imperative to ensure that the hatch distance is appropriately adjusted according to the laser beam diameter to uphold a particular overlap ratio. VED coupled with scanning strategies, has a direct influence on the shape, size, temperature, and cooling rates both within and around the melt pool. These defined printing parameters influence the residual stress and distortion of the final part.

2.7. Defects Classification In LPBF

Defects in L-PBF typically arise in finished parts through three primary pathways: (1) transfer of the initial feedstock powder, referred to as powder-related defects; (2) interaction between the laser, powder, and metal during melting, termed processing related defects; and (3) defects arising from post-processing treatments such as heat treatments.

Additionally, factors like equipment, build preparation, and part design can influence defect occurrence in additive manufacturing (AM) parts. Common defect types in metal AM encompass various forms of porosity like lack-of-fusion, keyhole, balling, and trapped gas, along with issues such as surface roughness, residual stress, and distortion (warping) due to the rapid solidification inherent in metal AM processes.

To mitigate defect formation in metal AM, it is crucial to understand and manage the mechanisms underlying defect generation through careful selection of materials, processes, and post-processing parameters. The subsequent sections delve deeper into the origins of defects, particularly focusing on the distinctive characteristics of various starting materials that contribute to defect formation.

2.7.1. Powder-Related Defects

Defects related to powder can significantly impact the quality and performance of the final product. These defects are often influenced by various powder characteristics including morphology, flowability, mean size, particle size distribution, and surface contamination. In additive manufacturing processes based on fusion, such as L-PBF or Electron Beam Melting (EBM), the properties of the powder are directly influenced by the method of powder production, which may include techniques like water and gas atomization, plasma atomization, or plasma rotating electrode process.

Spherical powders tend to offer advantages such as higher apparent density, better packing density, improved flowability, and smoother surface finish. However, the production cost of spherical powders is usually higher compared to other forms. In Powder Bed Fusion (PBF) processes, the use of a high fraction of fine powders (less than 5 μm) can lead to powder agglomeration, thereby negatively impacting packing density, flowability, and final part density.

The feedstock powder might harbor moisture, organic contamination on its surface, and/or trapped gases, adversely affecting the final part's quality. Porosity in the powder may transfer to the printed part, though it is unrelated to the direct interaction between the beam and powder.

2.7.2. Processing-Related Defects

Numerous studies have investigated the impacts of processing parameters such as power, scan speed, layer thickness, hatch spacing, and scan strategy on the formation of various defects, predominantly pores and voids. Specifically, the boundary for lack-of-fusion porosity hinges on the extent of overlap between melt pools.

Conversely, the keyhole porosity boundary corresponds to instabilities within deep keyholes, resulting in the closure of pores. A third boundary, termed the "beading-up" boundary, is determined by a blend of fluid flow patterns and capillary instability within the melt pool. This boundary poses a constraint on boosting production rates while upholding precision, for instance, by simultaneously increasing velocity and power in L-PBF AM systems [12].

Overall, the boundaries of lack of fusion (LOF), keyhole, and bead-up porosity define an effective process window for producing parts with nearly full density. Full density is quantified as samples possessing over 99.9% volumetric density, although large defects can still occur within this processing window (Figure 6). Other defects, such as cracking, distortion, and super-elevated edges, are influenced by the thermal history during printing and the printing patterns, which can be controlled by selecting an appropriate scan strategy and part design.

Mukherjee et al. [47] demonstrated that thermal strain can be managed by low heat input (low laser power, high scan speed, and small layer thickness). They concluded that alloys with lower heat capacity and higher thermal diffusivity are more prone to higher peak temperatures, larger pool volumes, and greater thermal strain. Among the three common alloys—nickel superalloy 718, Ti-6Al-4V, and stainless steel 316—thermal strain is relatively higher for alloy 718 and Ti-6Al-4V than for stainless steel 316 [47-48].

Another source of defects, known as spatters, is caused by ejected particles from the powder bed or liquid metal from the melt pool. There are two main reasons for solid/liquid metal ejections in L-PBF systems: (1) convective transport of liquid or vaporized metal out of the melt pool, known as droplet spatters, and (2) solid powder particles blown away by the heated cover gas, known as powder or sideway spatters [12].

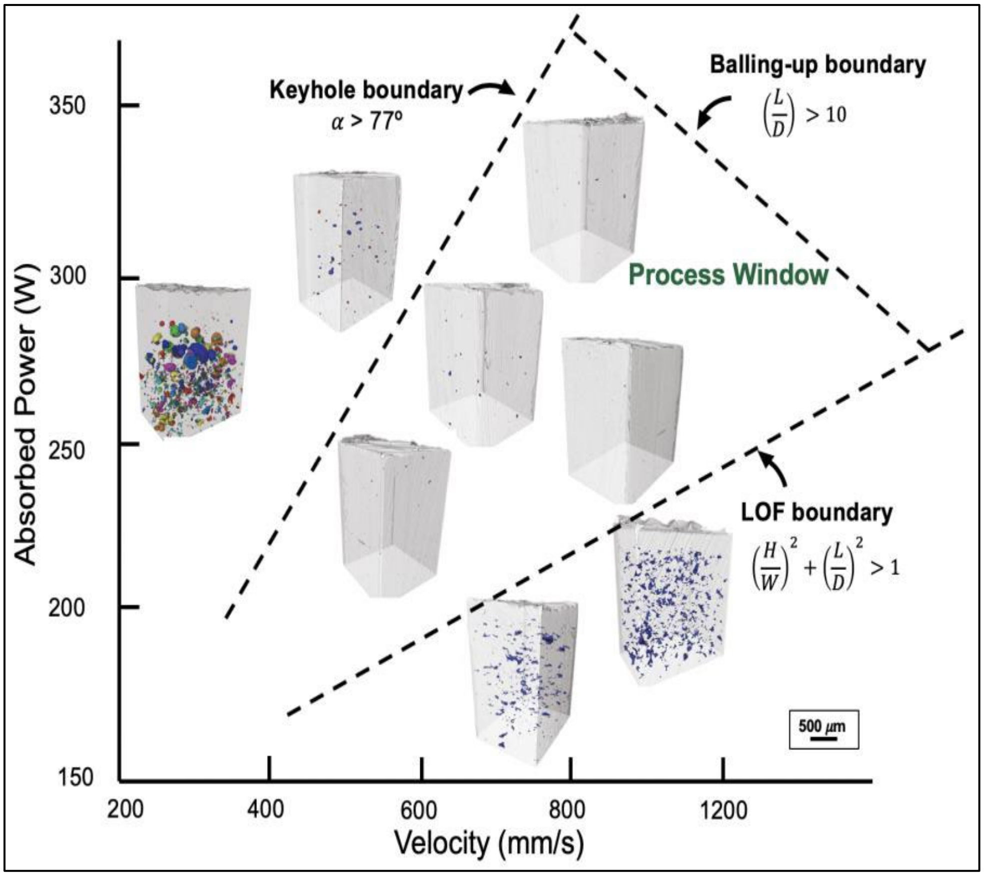

Figure 6: Defect Morphologies in L-BPF Metal AM [12]

2.8. Composition of AF96

AF96 is a military grade high performance low alloy steel with high ductility and high impact toughness. The elemental composition of AF96 low alloy steel includes molybdenum, manganese, vanadium, silicon, carbon, nickel, chromium, and significantly low impurities with iron being the balance. Table III below shows the elemental compositions of AF96 and their corresponding weight percent.

Table III: AF96 Composition by Weight[49]

Elements	**Composition by weight**
Iron (Fe)	Balance of composition
Silicon	1.50% or less
Molybdenum	0.50 to 1.50%
Vanadium	0.05 to 0.35%
Carbon	0.24 to 0.32%
Nickel	3.00% or less
Manganese	1.00% or less
Chromium	2.00 to 3.00%

2.8.1. Impurities in Composition

Impurities in alloys are mostly undesirable as they could have adverse effects on the alloy properties. However, impurities come with alloy production and therefore cannot be omitted from the bulk composition. Consequently, it is imperative to note that the amount of impurities in the bulk composition must be minimal to have less significant effect. AF96 has minimal impurities which include 0.025% or less of aluminum, 0.15% or less of nitrogen, 0.02% or less of calcium, 0.012% or less of sulfur, 0.20% or less of copper, and 0.015% or less of phosphorus [49].

2.8.2. Function of Individual Powders in AF96 Composition

Carbon plays a crucial role in the hardenability of AF96 alloy, contributing to its high strength and hardness. However, an excess of carbon negatively impacts the alloy’s toughness and sensitivity to quench cracks and defects, emphasizing the importance of carefully controlling carbon levels in the composition.

Similarly, manganese enhances alloy strength, but excessive amounts can lead to segregation and banding, forming undesirable secondary phases that affect both strength and toughness.

Chromium contributes to the alloy’s hardenability, high strength, and temper resistance, while molybdenum aids in solid strengthening, prevents embrittlement, and improves fracture toughness. However, excessive molybdenum can result in segregation and increased stabilization of bainite, impacting the alloy negatively. Molybdenum also aids in the stabilization of detrimental carbides at temperatures below the austenization transformation temperature.

Nickel ensures toughness even at extremely low temperatures. Excessive amounts of nickel offer no significant improvement except increased alloy cost.

Vanadium is an intentional addition to ensure high strength and hardenability to the alloy composition, preventing grain growth during high temperature treatment. Vanadium preserves the mechanical properties of the alloy by ensuring grain boundary pinning to prevent excessive grain growth during temperature heat treatment. Yet, an excess of vanadium can adversely affect work-hardening capability through carbide formation that in turn increases the yield/tensile strength ratio.

Addition of silicon decreases coarsening of epsilon carbide to cementite and enhances the toughness, hardenability and temper resistance of the alloy by preserving smaller semi coherent carbides. Silicon in excess affects hardness, strength, and ductility through over-stabilization of bainitic phases [49].

Like many alloys, iron serves as the balance in the AF96 alloy composition. The combination and precise amounts of these elements are crucial for achieving desirable properties such as ultimate tensile strength, yield strength, elongation to failure, impact toughness, or hardness in the alloy composition [49].

2.9. Powder Metallurgy

Methods for metal powder production can be categorized as follows:

1. Mechanical methods
2. Chemical methods
3. Physical methods

Any material can be transformed into powder by one or a combination of these methods. Selecting the appropriate methods depends on the specific application requirement and the intended properties and structure of the end product [50].

2.9.1. Mechanical Methods

Mechanical processes are not mostly employed as primary methods for production of metal powders. The mechanical comminution process is made up of various techniques like attrition, shear, and compression. The creation of metal powders by mechanical means hinges on combinations of these four fundamental mechanisms.

One prevalent approach involves employing a ball mill composed of a rotating drum containing durable, wear-resistant balls. The critical aspect lies in the rotation speed of the drum. Excessively high speeds cause material and balls to press against the drum walls due to centrifugal forces, hindering their relative motion. Conversely, too low a speed results in minimal movement within the lower part of the drum. The optimal speed entails elevating some materials and balls to the drums top, facilitating their descent onto the remaining materials.

Another type of mill is the vortex mill, fracturing material particles through mutual contact or collision. These mills feature rapidly rotating propellers within the casing and gas flow systems that extract the specific particle size fractions. However, a downside to mechanical methods is the potential for contamination from the mill walls and balls.

Flake metal powders stem from flattening equiaxed particles using alternate methods, employing ball, hammer, or roll mills. To prevent welding or adhesion, lubricants are introduced during milling. Aluminium, copper, bronze, silver, gold, iron, and stainless steel flake powders are commercially produced through these milling techniques [51].

2.9.2. Chemical Methods

Chemical reduction involves altering chemical compounds, often oxides but sometimes halides or other metal salts. This process can occur in solid, gaseous, or aqueous states. For instance, iron oxide can be reduced with carbon or tungsten oxide with hydrogen.

The Hogana process produces sponge iron powder, showcasing a batch approach where the ore remains stationary during reduction, unlike continuous methods. This technique relies on pure magnetite (Fe_3O_4) ores from northern Sweden, reducing the iron ore with a carbonaceous material. The process involves grinding the ore to specific particle sizes, placing it within cylindrical ceramic containers (saggers made of silicon carbide), and enveloping these containers with a mixture of coke and limestone.

These saggers are then arranged on cars and moved through a fuel-fired tunnel kiln, where carbon monoxide from the coke reduces the ore to iron. This reduction typically takes about 24 hours at 1,200°C. The limestone's role is to absorb any sulfur in the coke, preventing contamination of the iron. After mechanical removal from the saggers, the sponge iron is ground, and through magnetic separation, impurities are eliminated. Finally, the powder undergoes a continuous reduction in a hydrogen atmosphere on a stainless steel belt within a furnace [51].

2.9.3. Physical Methods (Atomization)

Atomization divides into categories namely, gas, water, and centrifugal. Almost any meltable material can turn to powder through liquid disintegration. Apart from chemical reactivity, which might require specific atmospheres or materials, the process disregards the typical physical and mechanical properties of the solid material. The method is widely used, particularly for producing high purity metals and pre-alloyed powders straight from the melt. The core technique involves pushing liquid through an orifice, often at the base of a crucible, and directing a gas or liquid stream onto the emerging melt. The orifices design heavily influences the outcomes, inducing melt turbulence that atomizes the material and swiftly reduces particle size by alloying the incoming gas or liquid.

Gas atomization yields typically spherical powders with smooth surfaces. Finer powders result from higher pressure and smaller jet distances. This method finds use in preparing powders for superalloys, titanium, high speed steel, and other reactive metals. However, it suffers from low overall energy efficiency (around 3%) and becomes costly if inert gases besides nitrogen are necessary.

Water atomization involves propelling a high-pressure water stream through nozzles to create droplets that collide with a metal stream. This method demands substantial energy to sustain the high-pressure water supply, estimating an overall process efficiency of 4% or less. It holds significance for producing low and high alloy steels, like stainless steels. However, due to oxide formation, it is not suitable for highly reactive metals such titanium and super alloys. Water atomized powders typically have irregular shapes and rough oxide surfaces.

Advantages of high-pressure water atomized powders include: reduced capital, enhanced purity, precise control over particle shape, size, and structure, consistent composition across all particles and flexibility in alloying. In water atomization, fine particles are preferred under conditions of low metal viscosity, low metal surface tension, superheated metal, low metal feed rate, high atomization pressure, and increased atomizing agent volume, velocity, and viscosity.

Figure 7 highlights key variables in the atomization process. Modifying particles shapes from nearly perfect spheres to highly irregular forms is achievable by controlling the processes between liquid metal stream disintegration and drop solidification. Spherical metal powders are favored by:

1. High metal surface tension
2. Extended flight paths
3. Lower jet velocity
4. Longer apex angles in water atomization
5. Elevated pouring temperature
6. Narrow metal range
7. Gas atomization, particularly inert gas

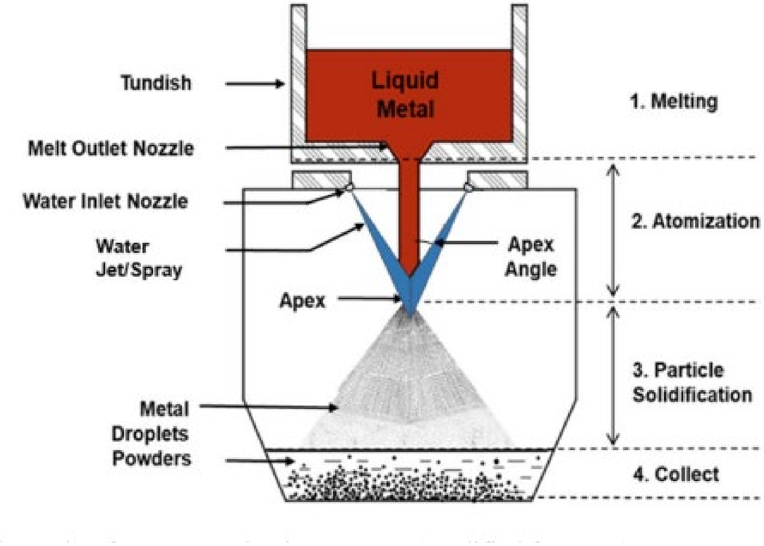

Figure 7: A Schematic Diagram of Water Atomization Process [52]

In water atomization, water pressures typically from 3.5MPa to 21MPa, with associated water velocities between 40m/s and 15m/s. The particle cooling rate falls within the range of 10,000K/s to 100,000K/s [51].

2.10. Mixing Methods for Powders

The first documented use of elemental mixing was conducted by Robert E. Schafrik in 1976. Schafrik observed the challenges of creating a titanium and aluminum alloy through conventional methods and pioneered the creation of titanium alloys via elemental mixing. Aluminum and titanium powders of known composition were combined using a Spex® Mill Mixer. The mixed powder was then placed into billet molds, melted, and extruded to produce specimens for testing. However, all the extruded samples exhibited cracks, voids, and delamination. Schafrik demonstrated that elemental mixing of metal powders was feasible but did not establish a completely satisfactory method for alloy creation. Schafrik emphasized the necessity of mixing powders in an inert atmosphere, as oxide formation was a significant cause of alloying failure [53].

Currently, Turbula® mixing is a widely accepted method for homogenously mixing powders of different compositions [54-55]. A Turbula® mixer operates through the rotation, translation, and inversion of the mixing vessel. Recent technological advancements have led to developing other mixing machines, including the Resodyn Acoustic Mixer – LabRAM II (LabRAM). An article published by Osorio et al. [56] analyzed the performance of mixing powders using a LabRAM. Osorio et al. found that homogeneous mixes of pharmaceutical powders could be effectively achieved. However, the most significant drawback to the LabRAM mixing method, as identified by Osorio et al., was the limited quantity of powder that could be mixed in a single batch. They concluded that inadequate mixing could occur with improper process parameters, emphasizing the importance of selecting appropriate mixing parameters [56].

Li et. Al. [57], created four iron-chromium-nickel alloys using a Turbula® mixer and elemental powders. Maintaining a 30% powder to mixing container volume ratio, each mixture was blended in the Turbula® for 30 minutes. Microscopic imaging was performed on the samples after mixing to analyze the homogeneity of the mix. Energy dispersive X-ray spectrometry (EDS) images revealed a diverse range of powder shapes and sizes, randomly distributed throughout the mixture. The randomly distributed shape and sizes established that the powder was adequately blended. Direct energy deposition (DED) was employed to fabricate samples measuring 50.8 × 12.7 × 6.35 mm. The DED process utilized a large-diameter laser beam and a powder feed system driven by a gas, such as argon, flowing through the powder feed tube. Specimens were produced using two different particle size distributions. Although both distributions encompassed the same overall particle size range, one distribution featured larger chromium particles, while the other had larger nickel particles [57].

Takeda et. al. [58] performed experiments using laser cladding. Laser cladding is a process similar to Directed Energy Deposition (DED). Takeda et. al. used this process to create iron, chromium and nickel alloys. The powder feedstock for these experiments was prepared using various methods, involving one, two, or three powder hoppers. In the one hopper configuration, the feedstock consisted of an elemental mixture of powders. In the two-hopper setup, both hoppers contained identical elemental mixtures. The three hopper configuration involved each hopper containing a different elemental powder. Stepper motors were utilized to control the feed rates of powder from each hopper across all experimental setups. The study emphasized the significance of travel speed, noting that the uniformity of deposits relied on the deposition travel speed. Higher travel speeds resulted in smaller, less homogeneous deposits, whereas slower travel speeds yielded larger specimens with greater homogeneity [58].

Zhao et al. [59] prepared powders for L-PBF process using a tumble mixer. Nickel-tin samples were produced with the SLM process. The elemental powders were mixed in proportions matching the target alloy for four hours in a tumble mixer and then dried for twelve hours to eliminate moisture. A Realizer GmbH SLM 250 printer was used to print 5 mm cubes. Zhao et. al found that although the powder was adequately mixed and homogeneous, the samples contained both process and material related discontinuities. Several cracks and pores were observed throughout the cubic specimens. It was determined that these cracks were not due to the cooling rate during printing but were attributed to the poor strength of the alloy and the high residual stress induced by the L-PBF printing process [59].

2.11. Dry Metal Alloying

Dry Metal Alloying (DMA) of metal powders involves the mixing of elemental metal powders using the LabRAM mixer. The patent-pending process was developed by the Montana Tech Advanced Manufacturing research group to produce DMA powders composed of various elemental and ferro-alloyed powders of precise composition and quantity. Utilizing the Dry Metal Alloying method provides an advantage over commercial-grade (pre-alloy) alloy reliance. Where the DMA composition and quantity can be easily adjusted to suit a specific research objective. Elemental and ferro-alloyed mixing in the LabRAM mixer results in a dry bulk composition equivalent to standardized commercial-grade metal alloys [60].

2.12. Phase Transformation of Low Alloy Steels Welds

The basis for understanding physical processes that come about in fusion welding of low-alloy steels is needed to design reliable and economical welding processes. The physical processes are categorized as evaporation of alloying elements in steel, dissolution of gases from arc atmosphere, oxide inclusion formation, solidification, solid state transformation and generation of residual stresses [61].

A longstanding debate surrounded the interpretation of steel microstructures because elements within the same primary structure might exhibit varying appearances depending on the observation plane. Additionally, certain structures, despite similar morphological traits, can possess distinct mechanical properties. Consequently, the terminology used to describe microstructural constituents in weld metals was historically convoluted, employing different terms for identical constituents.

This confusion prompted the International Institute of Welding (IIW) to devise a comprehensive microstructure quantification system in the 1980’s. This scheme aimed to facilitate the identification of constituents via optical microscopy. Thewlis provided an overview of the IIW scheme, focusing on the primary structures formed during reconstructive and displaced transformations in steels. However, there remain unresolved queries concerning reaction kinetics, particularly pertaining to elucidating the growth mechanisms of bainite.

Such clarity could significantly enhance the accuracy in differentiating bainite from other phases. A critical review to address the confusion prevalent in the literature regarding bainite and acicular ferrite was conducted. The following describes the microstructure development of a low alloy steel.

1. Primary ferrites nucleate at the prior austenite grain boundaries, known as allotriomorphic ferrite, and to a lesser extent within austenite grains, referred to as idiomorphic ferrite, where non-metallic inclusions (NMIs) are present. Allotriomorphic ferrite arises between 1,000 and 650°C, while ferrite side plates, separated by low angle boundaries, develop between 750 and 650°C, also at the prior-austenite grain boundaries.
2. Acicular ferrite nucleates heterogeneously on the surface of NMIs during the austenite-ferrite transition, resulting in chaotic crystallographically disoriented plates, typically 5 to 15µm in length and 1-3µm in width. Some authors distinguish primary and secondary acicular ferrite, stating that primary acicular ferrite plates nucleate on NMIs, whereas secondary acicular ferrite forms through sympathetic nucleation. However, there is a contention that certain parallel laths reported as formed through sympathetic nucleation in continuous cooling studies might be bainite laths. The temperature range for acicular ferrite formation typically falls within 750 to 560°C, contingent upon the composition and cooling rate.

3. Bainite develops as separate plates or sub-units, forming sheaves of parallel ferrite laths categorized as upper or lower bainite based on the transformation temperature. In upper bainite, carbon precipitates as cementite (Fe_3C) between ferrite plates, while in lower bainite, carbon becomes supersaturation with carbon, leading to carbide precipitation within and between ferrite sub-units. The bainite start temperature is around 560°C, but this can vary based on composition and cooling rate. In certain low alloy steel weld metals, the non-metallic inclusions function as effective nucleation sites for bainite, resulting in intragranular bainite colonies resembling acicular ferrite in appearance, causing confusion in optical microscopy.
4. Pearlite transformation occurs at austenite grain boundaries or inclusions. At higher temperatures, pearlite forms nodules with coarse alternate ferrite and cementite lamellae, gradually becoming finer with decreasing transformation temperatures. At extremely low temperatures the lamellae may appear irresolvable under a light microscope, resembling a ferrite or carbide aggregate. Lamellar pearlite, FC(P) in the IIW classification, might be mistaken for martensite if the ferrite or cementite plates are irresolvable under a light microscope.
5. Martensite arises from a rapid and diffusion less transformation, retaining carbon in solution. It manifests as laths or plates, with lath martensite showing a substructure characterized by dislocations arranged in cells and plate martensite exhibiting exceptionally fine twins known as twinned martensite [36].

The schematic diagram in Figure 8 shows the various phase changes that occur as a function of weld cooling, in the weld metal region. The weld pool region typically reaches temperatures as high as 2,500K. During the cooling process:

- Between 2,300 to 1,800K, for (I), the liquid steel sees a reaction between dissolved oxygen and deoxidizing elements, resulting in the formation of intricate oxide inclusions within the 0.1 to 1 µm size range.
- From 1,800 to 1,600K, for (II), solidification into ferrites initiates, and envelopes these oxide inclusions, followed by the transition into austenite.
- In the temperature range of 1,100 to 500K, for (IV-VII), austenite undergoes transformations into various ferrite structures, including allotriomorphic ferrite, Widmanstatten ferrite, and acicular ferrite.

Maximizing the presence of acicular ferrite in steel welds leads to achieving the ideal combination of strength and toughness. It is a widely recognized fact that inclusions within steel welds play a crucial role in fostering the development of acicular ferrite. Consequently, there is a significant need to comprehend the inclusion formation in liquid steel and its effect on transformation of austenite to various ferrite morphologies.

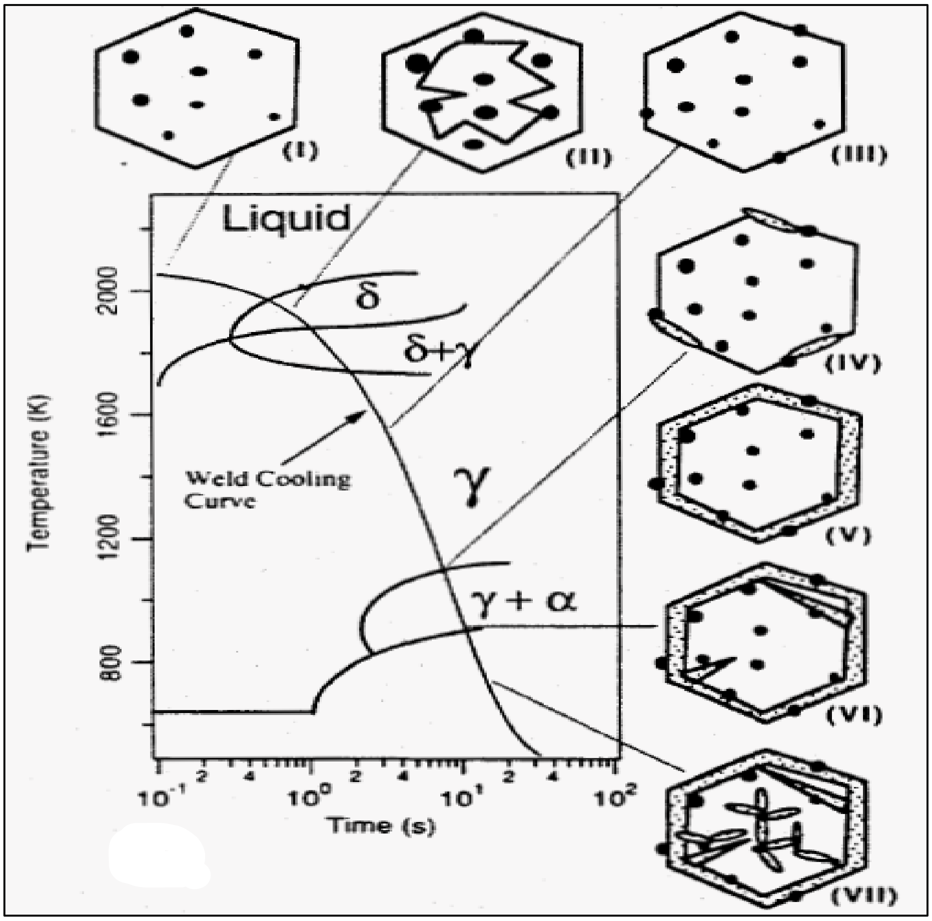

Figure 8: "Schematic Diagram of Continuous Cooling Transformation Diagram Showing the Development of Weld Metal Microstructure in Low Alloy Steels. (I) inclusion formation, (II) solidification of liquid to ferrite, (III) fully austenitic structure, (IV) [61]

The microstructure of a low alloy, low carbon steel weld metal is shown in Figure 9. Figure 9 shows the grain boundary ferrite (A), Widmanstatten ferrite (C), and acicular ferrite (D), while Figure 10b shows the upper bainite (E), lower bainite (F) and a polygonal ferrite (B). To identify the upper and lower bainite a transmission electron microscope (TEM) is usually needed for the examination [62].

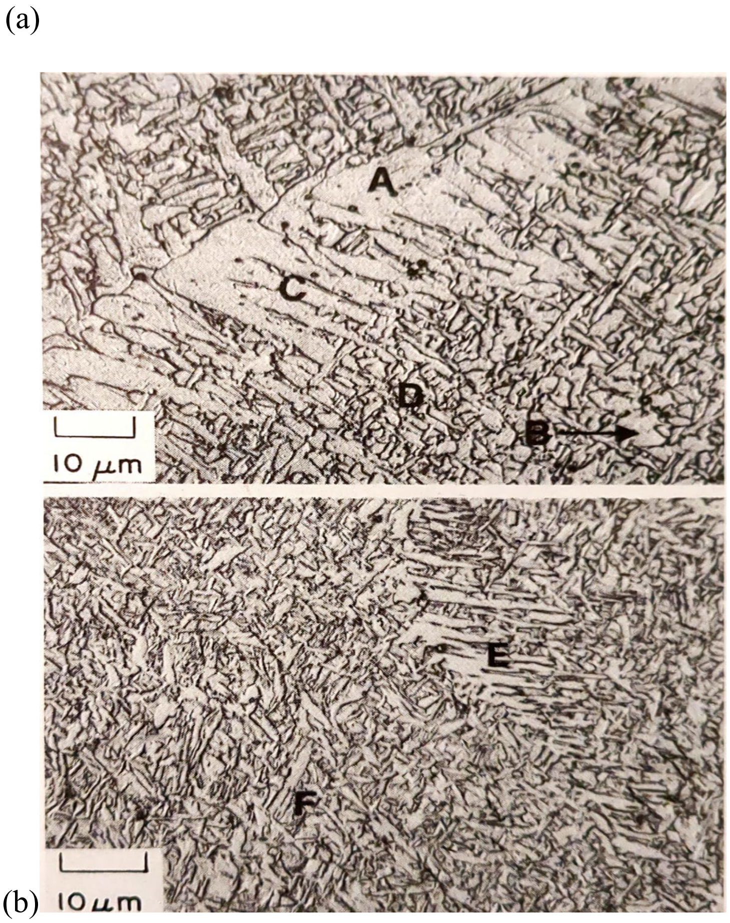

Figure 9: Micrograph Showing the Microstructures for a Low Alloy Steel Weld Metal: A, grain boundary ferrite; B, polygonal ferrite; C, Widmansatten ferrite; D, acicular ferrite; E, upper bainite; F, lower bainite [62]

3. Materials and Methods

3.1. DMA Constituent Powder

The DMA constituent powder blend used in this study was produced by four different gas atomized commercial grade alloys and powder manufacturers. These alloys are H13, 420 stainless steel, 4340 steel, ferro-nickel, ferromolybdenum, and iron powder. These alloys were chosen as the constituent because they had the chemical compositions for AF96 alloy especially vanadium, silicon and carbon which were difficult to procure. The H13 powder was produced by Carpenter Additive, the 420 stainless steel, 4340 steel, and ferro-nickel powder by GKN Powder Metallurgy, ferro-molybdenum by Ervin industries, and the iron powder by Atlantic Equipment Engineers.

3.2. Particle Size Distribution

The particle size distribution (PSD) of powder feedstock significantly influences layer thickness and packing density. It determines the printing precision, surface quality, and density of printed components [63-67]. Common methods for measuring PSD in additive manufacturing (AM) metal powders include microscope observation, sieving analysis, and dynamic light scattering [68].

Microscope observation employs equipment such as optical and scanning electron microscopes (SEM) to observe and measure the morphology and particle size distribution. This study utilized sieving analysis to evaluate PSDs, allowing powder particles to pass through a series of sieves with progressively smaller mesh sizes. The weight of the particles retained on each sieve is then recorded and calculated as a fraction of the total mass [69].

The PSDs for all six powders were analyzed in accordance with ASTM B214 Standard using a sieve stack of 11 sieves with mesh sizes ranging from 20 to 150 µm. The group of sieves were assembled with the largest materials at the top. A collecting pan was added to the bottom of the finest sieve (20 µm).

The sieve stack assembly was fastened and placed in a LabRAM mixer. The RAM operates at a 60 Hz power and accelerates axially up to 100 gravitations (g’s) of acceleration. For this application, the sieving was performed at 10 g’s for 5 min. Ferromolybdenum was re-sieved into the required size fraction of 15 to 53 µm.

3.3. Powder Morphology

In LPBF, the effect of powder morphology is crucial to the resulting part density, mechanical properties, and surface quality of the final part as well as the processability of the powder itself [70]. Powder morphology was analyzed using a TESCAN MIRA3 TIMA machine equipped with an EDAX electron backscatter diffraction detector by AMETEK.

A double-sided carbon tape was placed onto a stub. A thin layer and representable amount of powder particles were collected onto the surface of the carbon tape. The stub was gently tabbed and blown with an air duster to remove excess sample before placement in the machine for analyses.

3.4. DMA Powder Composition

The constituent alloys used were carefully selected, considering the chemical composition of each which should fit AF96 alloy composition. The chemical composition and respective weight percent for all the powders were provided by the manufacturers; chemical compositions for H13 powder, 420 stainless steel and 4340 steel are shown in Table IV. The ferro-nickel powder had a 50% iron and 50% nickel composition by weight percent and the ferro molybdenum had 60% iron and 40% molybdenum composition by weight percent.

Table IV: Chemical Composition of H13, 420 Stainless Steel and 4340

Powders/ Alloying Elements	**Constituent Powder (wt.%)**		
	H13	**420 SS**	**4340**
Carbon (C)	0.32	0.29	0.41
Vanadium (V)	1.00	-	-
Molybdenum (Mo)	1.34	0.02	0.2
Chromium (Cr)	5.18	12.1	0.9
Silicon (Si)	1.15	0.59	0.3
Manganese (Mn)	0.30	0.68	0.8
Nickel (Ni)	0.1	0.28	1.9
Iron (Fe)	Balance	Balance	Balance
Copper (Cu)	0.03	-	-
Nitrogen (N)	0.04	0.01	-
Sulphur (S)	0.01	0.029	-
Phosphorus (P)	0.01	-	-
Oxygen (O)	0.02	0.03	-

3.5. AF96 DMA Mixing

3.5.1. Phase One

A composition calculator was designed in excel to calculate, control, and measure the amount in weight percent and grams needed for a DMA mix of AF96 alloy. The DMA constituent composition of AF96 alloy, as per the USAF96 Patent, is detailed in Table IX of Appendix A. Adjusting proportions in the mix composition allows for precise control of elemental composition in weight percent, resulting in a calculated mass of 100g for the batch mix.

The AF96 powder blend was mixed in an 8 oz fluid vessel. A 700g batch of DMA AF96 constituent powders occupied about 75% of the vessel, leaving enough space for the powder particles to agitate and mix well in the vessel. As shown in Figure 10, the constituent powders of the specific weights according to the composition mentioned in Table X of Appendix A, were poured into the mixing vessel one above the other in a specific manner. Finer particle sized powders were placed at the bottom and vice versa. This counts significantly towards creating a homogenous mixture as the finer particles rise through the mixture during acoustic mixing.

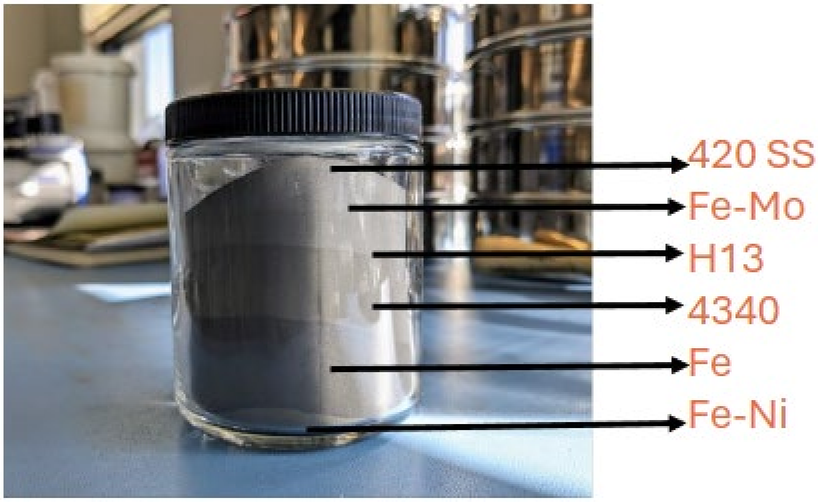

Figure 10: 8-fluid-ounce Mixing Fluid Vessel Containing Constituent Metal Powders Before Mixing

3.5.2. Mixing Parameters

The 8-fluid ounce (fl.oz.) vessel containing the powder constituent was sealed with a tape on the lid to prevent the lid from loosening and particles from falling out during agitation of the powder. As shown in Figure 11, a silicone pad was placed between the bottom of the vessel and the base of the RAM and between the clamp and the top of the vessel to ensure vibration damping during mixing in the RAM. Mixing for this application was performed at 30 g’s of acceleration for 4 minutes.

Figure 11: Mixing Vessel for DMA AF96 in RAM

3.6. DMA AF96 Powder Characterization

3.6.1. X-Ray Fluorescence Spectrometry (XRF)

XRF Spectro analysis was performed on the DMA compositions using an AMETEK Spectro XRF machine. The analyses were performed for two DMA compositions. Five samples were drawn from each compositions with a sample thief. The samples were drawn from five different locations of the 8 oz mixing vessel (Figure 12). The samples were drawn from both the top and bottom half of the mixing vessel. Three tests were conducted on each sample and the results were averaged.

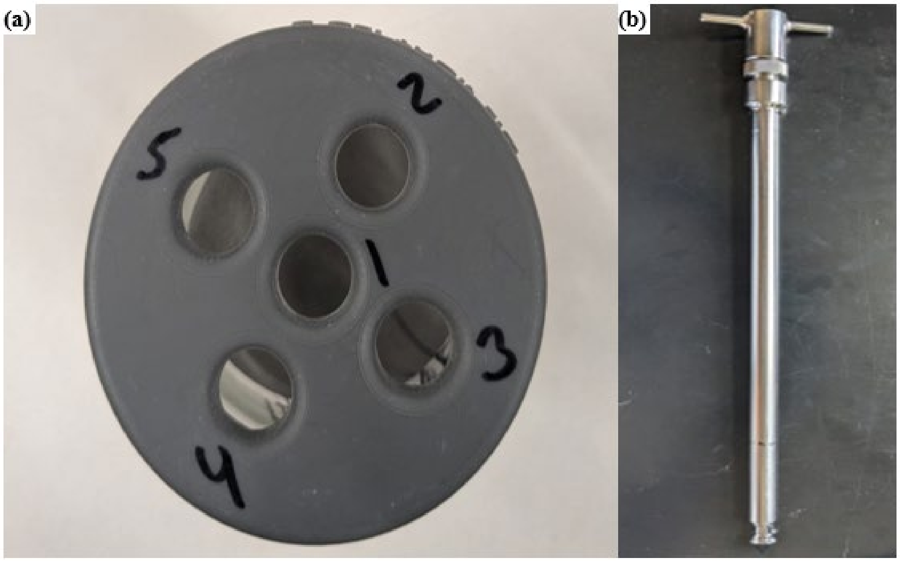

Figure 12: (a) Sampling Lid Showing Five Different Sampling Positions, (b) Sampling Thief

3.7. Preliminary Printing Investigations

3.7.1. ONE Click Metal Printer

Printing was performed by a commercial One Click MPRINT Printer (Figure 13a). The MPRINT is a 200 W fiber laser machine with a focus diameter of 70 µm enhanced by a Galvo scanner and a scanning speed of about 3,000 mm/s. The five-cartridge powder system enables safe and clean powder handling while minimizing direct powder contact for the user. A cartridge can hold 2.5 kg of powder, and five cartridges of powder can build a part of 150 mm height.

The MPRINT is incorporated with a large build volume of 150 mm × 150 mm × 150 mm construction area and can build with a powder layer height of 20 to 80 µm. The process chamber has a gas extraction tube that collects fumes in the built chamber to prevent powder contamination. A powder doser system with a coater (moving from left to right) spreads the powder onto the substrate plate to ensure a continuous powder flow during the build process.

An overflow cartridge collects excess powder from the overflow during the build process. After printing the 3D part in the build module is transferred to the MPURE (Figure 13b) to remove loose particles surrounding the built part. The MPURE serves as an unpacking area for printed parts and sieving station for used powder.

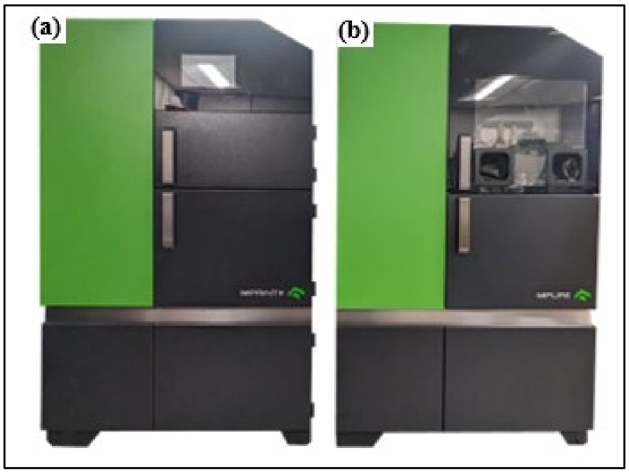

Figure 13: (a) Commercial OneClick MPRINT Printer, (b) MPURE System

3.7.2. Phase One Printing Parameters

The printing parameters for the DMA AF96 powder were inferred from [71] where L-PBF printing parameters were developed for commercially produced AF96 metal powder.

Phase one of the experiments was the exploration stage to determine the effect of the different printing parameters on the final printed AF96 deposits. Nine AF96 cubes were printed at three different power settings of 200 W, 180 W and 160 W. A constant layer height of 40 µm and 100 µm hatch spacing was selected. Figure 14 shows how the cubes were positioned on the build plate according to their process parameters. As seen in Figure 14 the linear energy density increases across the build plate as travel speed decreases.

Figure 14: Schematic of Printing Parameters for Preliminary Investigation

The linear energy density was established from an important variable in L-PBF known as the volumetric energy density as discussed in the background of this thesis paper. The linear energy density is a simplified variable used to predict the porosity and microstructure of printed parts. The linear energy density is utilized because it enables quantitative comparisons between parts produced with different laser parameters, particularly during the initial stages of process parameter exploration for fabricating dense parts.

3.7.3. Arc-Spark OES

Arc spark OES was performed on a Spectro MAXX machine from AMETEK to analyze the chemical composition of the AF96 printed deposits. Nine samples were analyzed. Three tests were performed on each sample and all results from the tests were averaged.

3.7.4. Sample Preparation

After printing, the AF96 cubes of 19.05 mm height and 15.86 mm width were sectioned by a wet abrasive saw along the x, y, and z planes. The sectioned samples were hot-mounted in a phenolic using the LECO MX400 Mounting Press machine (Figure 15). The target surfaces were prepared using standard metallographic procedures. The surfaces were polished with silica carbide grits sizes of 180, 320 and 600 accordingly.

The final polishing procedure to remove stresses and scratches from the surface involved polishing with 6- and 1-μm diamond suspensions, respectively. The samples were run through ultrasonic sonicator baths to remove any debris. Deionized water (DI) was used to rinse and clean the samples to remove any trace contaminants that could affect the experiment.

Once the samples are rinsed with DI water, they undergo rinsing one more time with a 99% alcohol based isopropyl solution for disinfection and further cleaning. The AF96 alloy contains many alloying elements including carbon, a major alloying element. Hence, for the EDS analysis to measure the weight percent of the elements, the samples had to undergo gold coating to make the carbon element especially visible during the analysis.

3.7.5. SEM-EDS Line Scans

Scanning electron microscopy and energy dispersive spectrometry (EDS) were carried out on the x plane (Figure 15) of all samples to analyze the homogeneity of the powder mix during melting. Six EDS line scans were performed to measure the chemical composition of the samples. Relative standard deviations of the line scans results were calculated and compared to the travel speed and linear energy density.

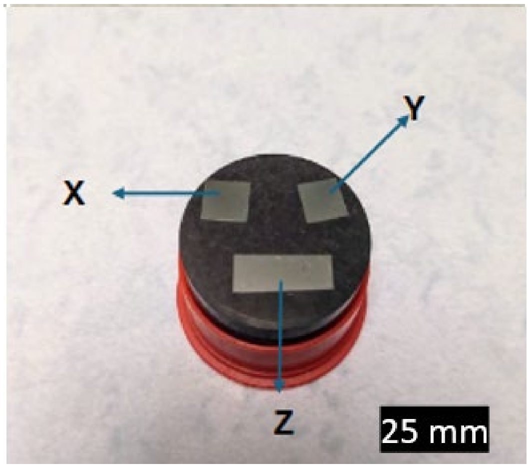

Figure 15: Sectioned and Hot Mounted AF96 Samples Showing X,Y, and Z Planes

3.8. Mechanical Testing

Rockwell hardness measurements at scale C were performed using a Mitutoyo HR-400 Rockwell hardness testing machine. A diamond indenter was utilized at a total test force of 150kgf. Hardness tests were performed on three different spots of the samples x-plane. Eighteen samples from phases one and two were analyzed and the averages were plotted against the linear energy density.

3.9. AF96 DMA Mixing and Printing Parameters for Phase Two

This phase of experiments was designed to address the compositional anomalies during phase 1 and optimize process parameter based on the results from phase 1 experiments. The focus of improvement was mainly on the DMA powder composition and L-PBF deposits after arc spark spectrometry analyses indicated a high Mo and low carbon content.

The actual wt.% for molybdenum was reduced by correcting the Mo composition for H13 from 1.30wt.% to 1.34wt.%. The wt. % for carbon was also increased on the composition calculator to create a second composition (Table XI, Appendix A). The irregular iron powder suspected to affect the results of the DMA deposits was reduced from 32.52 grams to 19.64 grams in composition two (Table XI, Appendix A).

To optimize the printing parameters, the linear heat input was increased across the build plate by reducing the travel speed while maintaining the same laser power settings at a constant 40 µm layer height and 100 µm hatch spacing (Figure 16).

Figure 16: Build Strategy for Phase 2 Experiments

4. RESULTS AND DISCUSSION

4.1. Particle Size Distribution and Morphology Analysis

PSD analyses and particle morphology were performed on all the constituent powders using sieving and SEM analyses to ensure that the particle sizes were within the required and accepted range for L-PBF process on the One Click MPRINT printer. Reported results as shown in Figure 17 indicate that most of the individual constituent powders were within 53 to 15 µm.

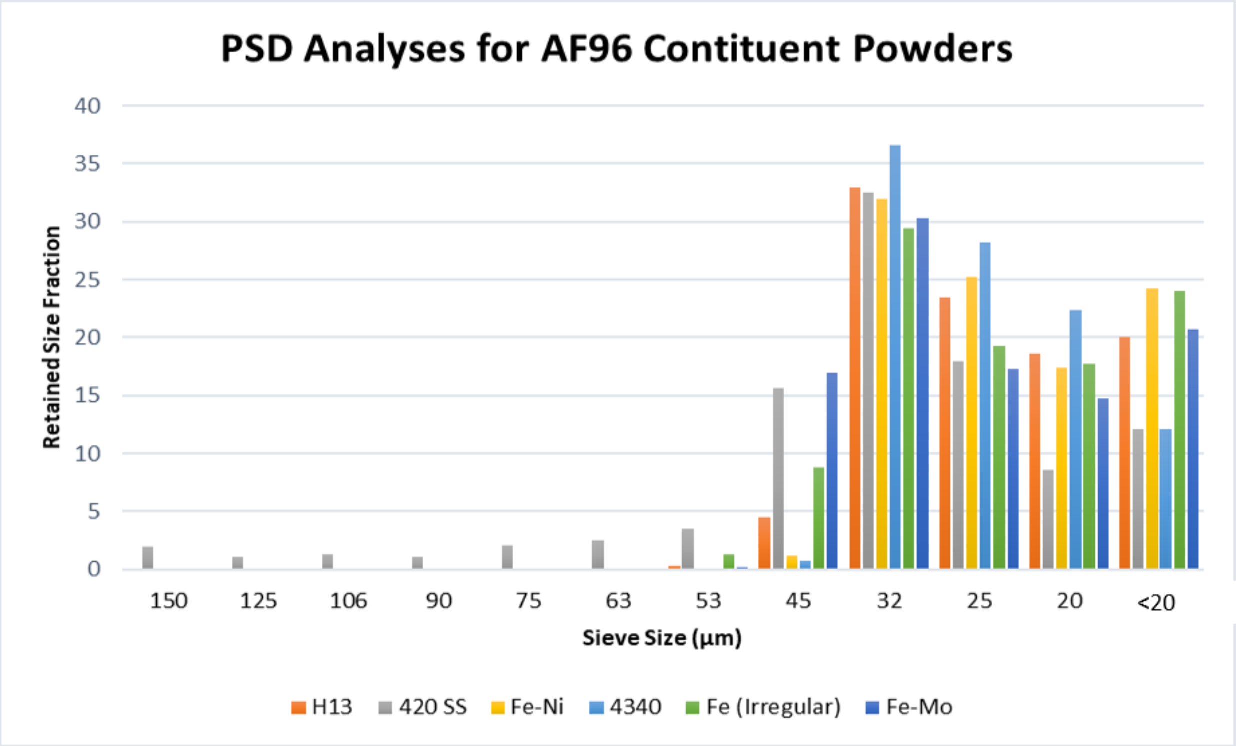

Figure 17: PSD Analysis for AF96 Constituent Powders

Powder particle morphology and PSD analysis gave a greater insight into the powder characteristic than just PSD alone. PSD and morphology of the metal powder is crucial to flowability, and the quality of the resulting powder bed formed in the PBF process. Table V presents the resulting D10, D50 and D90 values of the constituent powders.

Table V: PSD Results for Constituent Powders

Constituent Powder	**D10 (µm)**	**D50 (µm)**	**D90 (µm)**
H13	<20	30	44
420 SS	<20	32	63
FeNi	<20	25	32
4340	<20	28	42
Fe (Irregular)	<20	27.5	45
Fe-Mo	<20	32	47

Figure 18 shows the SEM micrographs of the iron powders for DMA AF96 bulk composition. The SEM micrographs confirmed the particle morphology of the metal powders as indicated by the manufacturers. All constituents metal powders indicated spherical morphology except for iron which was irregular.

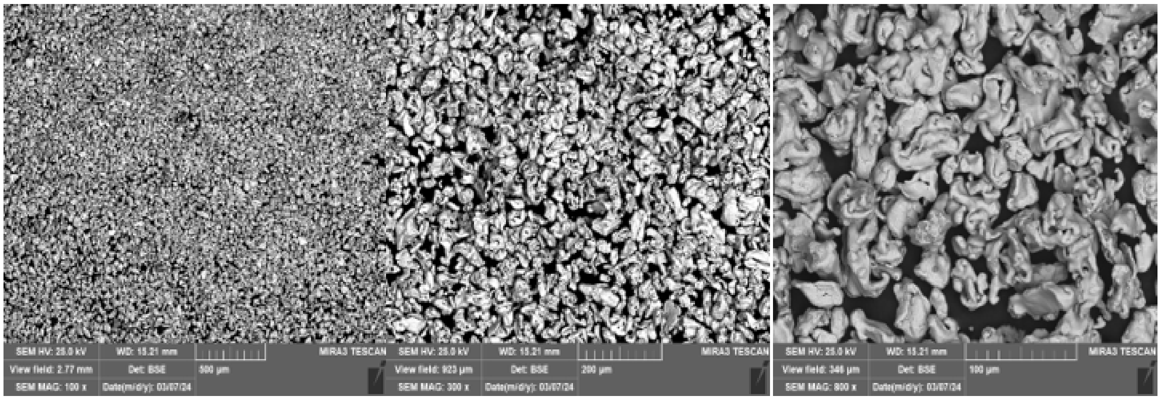

Figure 18: SEM Micrograph for Irregular Iron Powder at 100X, 300X, and 800X

The irregular iron powder was not the only iron element in the bulk feedstock. The remaining alloy composition had iron mainly as the balance of the composition.

The H13 powder in Figure 19 was generally and consistently spherical with few angular powder particles. Fifty percent of the particles were smaller than 30 µm, and ninety percent of the particles were smaller than 44 µm.

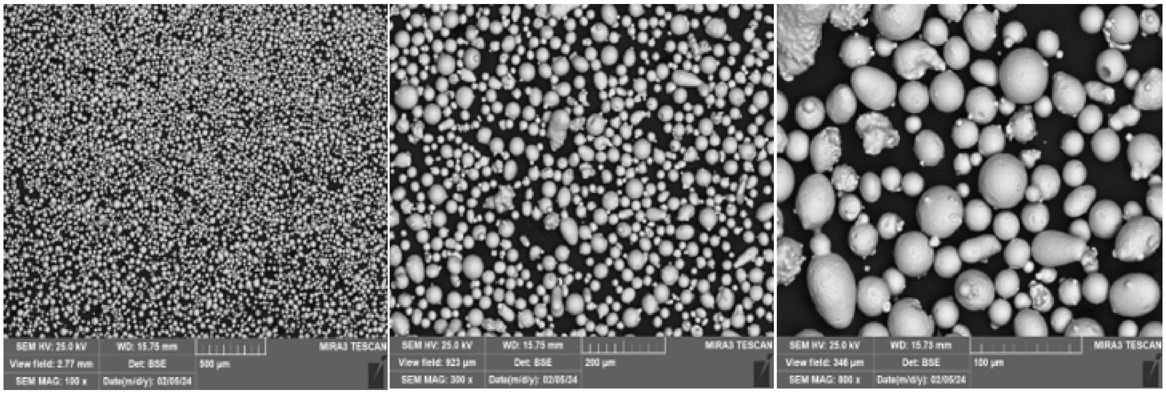

Figure 19: SEM Micrographs of H13 Powder at 100 X, 300X and 800X

The 420 stainless steel powder had larger spherical particles than the H13 powder particle (Figure 20). As mentioned in Table V, ninety percent of the particles for 420 stainless steel are less than the size of 63 µm compared to 44 µm for H13 powder.

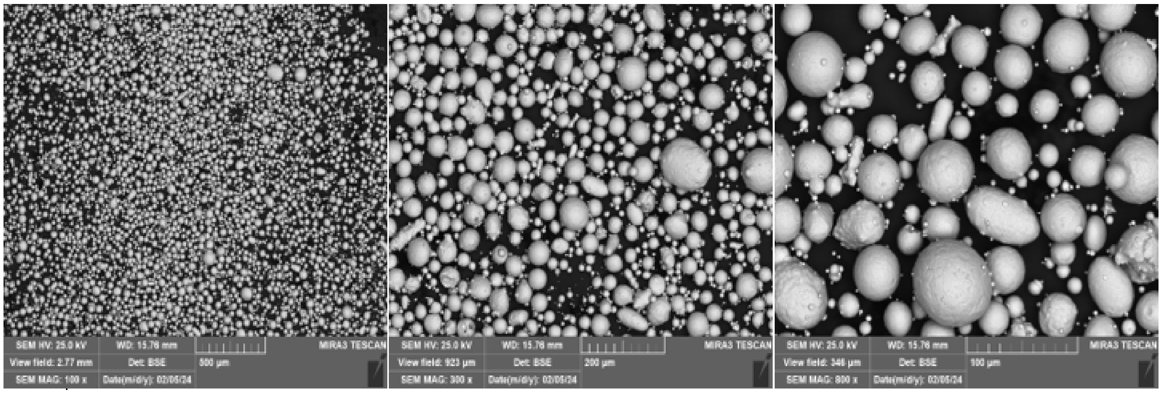

Figure 20: SEM Micrographs of 420 Stainless Steel Powder at 100 X, 300X and 800X

The ferronickel powder had the smallest particle size distribution. Ninety percent of the particles were smaller than 32 µm and 50% of the particles were smaller than 25 µm as seen in Table V and Figure 21. The particles were consistently spherical in shape. As seen in Figure 21, the ferronickel powder also exhibited few elongated particles than the other spherical powders. The ferronickel powder had a 50-50 composition of iron and nickel.

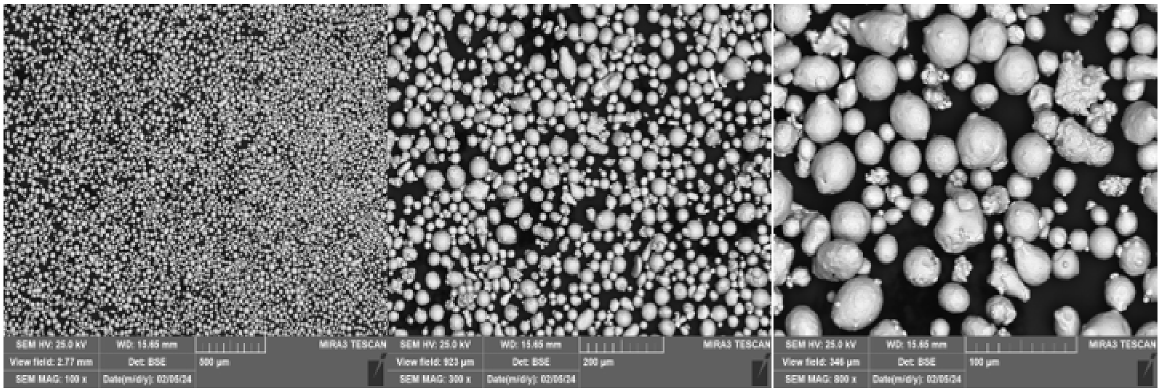

Figure 21: SEM Micrographs of Ferronickel Powder at 100 X, 300X and 800X

The ferromolybdenum powder had a D50 of 32 μm, similar to that of 420 stainless steel and the second highest D90 of 47 μm. The ferromolybdenum powder had a 60-40 composition of iron and molybdenum. As seen in Figure 22, the morphology of the ferromolybdenum particles was mostly spherical with fewer fractured particles.

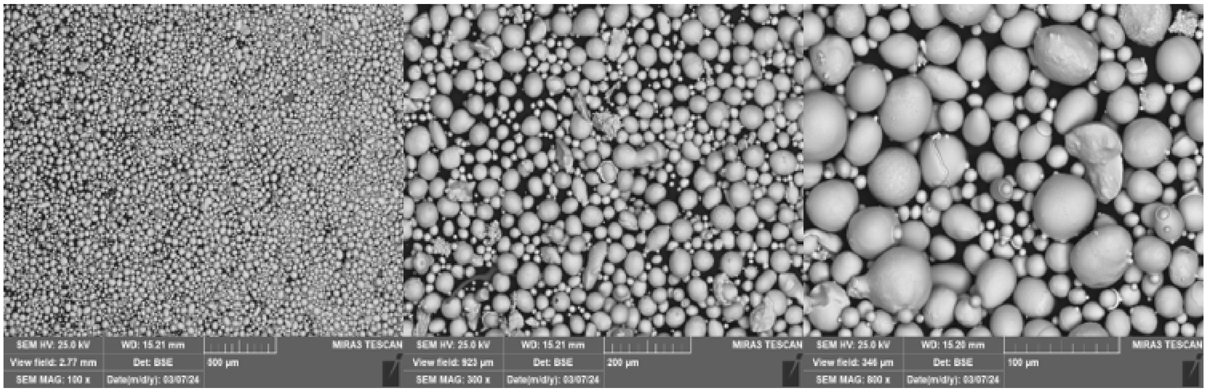

Figure 22: SEM Micrographs of Ferromolybdenum Powder at 100 X, 300X and 800X

The 4340 steel powder had a D50 of 28 μm with 90% of the particles smaller than 42 μm. As depicted in Figure 23, the 4340 steel powder contained spherical particles along with few elongated and angular powder particles.

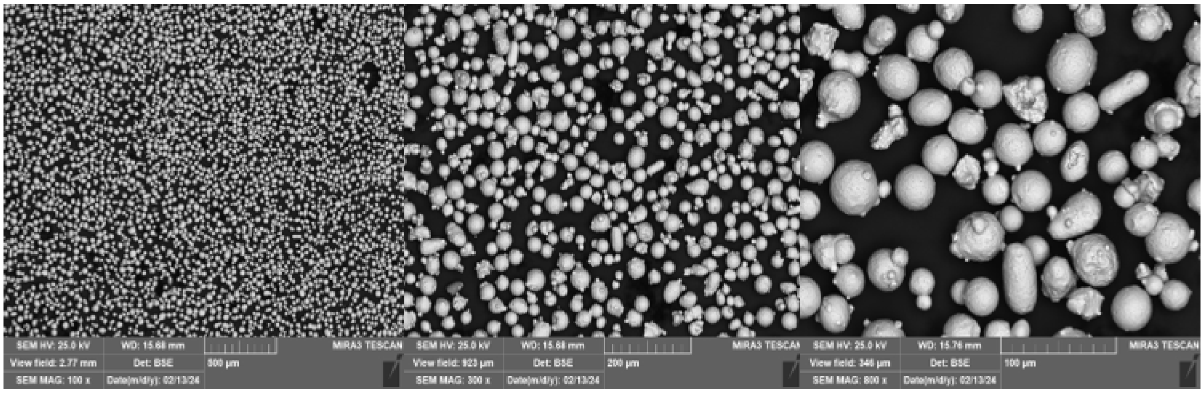

Figure 23: SEM Micrographs of 4340 Steel Powder at 100 X, 300X and 800X

4.2. PSD and Morphology of DMA AF96 Alloy

Figure 24 shows the particle size distribution analyses for the DMA AF96 feedstock powder. According to the sieve analysis results, the D10, D50, and D90 was calculated to be <20 µm, 27.5 µm, and 42 µm respectively. A uniform mix and distribution of powder particles is noticed in the morphology of the DMA AF96 powder.

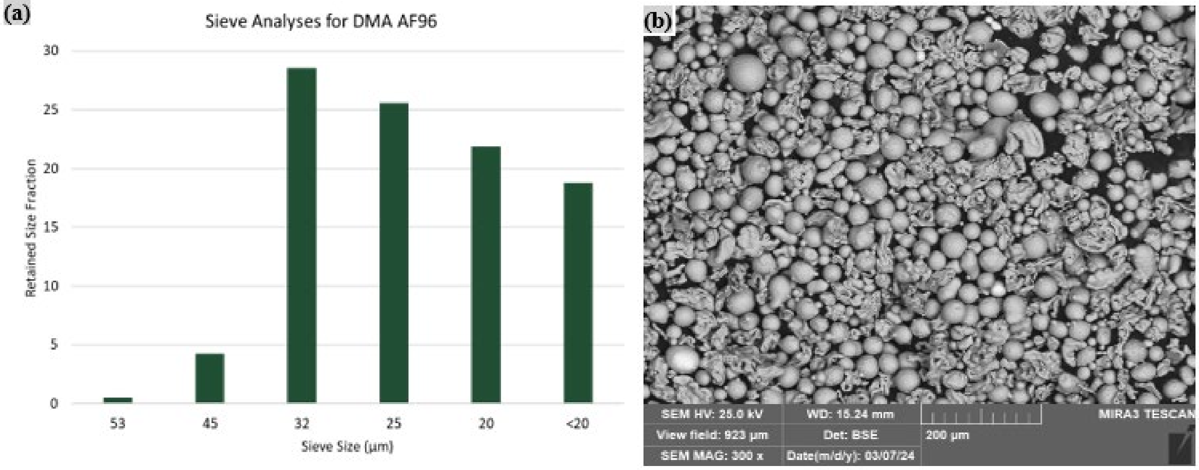

Figure 24: PSD (a) and Morphology (b) of DMA AF96 Alloy

4.3. X-Ray Fluorescence Spectrometry (XRF) Analysis

Results from the XRF analyses on composition one and two are compiled in Table VI. The results for composition 1 were consistent with the target composition except for molybdenum which was high. It was later determined that the molybdenum composition (1.30 wt.%) for H13 powder on composition 1 (Table X , Appendix A) did not correspond to the actual composition (1.34 wt.%) on the data sheet from Carpenter additive manufacturing. XRF tests cannot detect light elements, as a result carbon was not detected during these analyses. The powder mixing process was optimized to correct the high composition of molybdenum for composition two. The wt.% for all elements in composition two were consistent with the target composition.

Table VI: XRF Results for DMA AF96 Composition One and Two

Elements	**Composition 1 wt.% (Phase 1)**	**Standard Deviation (Phase 1)**	**Composition 2 wt.% (Phase 2)**	**Standard Deviation (Phase 2)**	**Target Composition wt.%**
Si	0.534	0.03	0.489	0.03	1.50 or less
Mn	0.500	0.03	0.503	0.03	1.00 or less
Cr	2.439	0.09	2.252	0.09	2.00 to 3.00
C	-	-	-	-	-
Mo	1.629	0.15	1.332	0.09	0.50 to 1.50
Ni	2.545	0.19	2.665	0.16	3.00 or less
V	0.248	0.01	0.201	0.01	0.05 to 0.35
Fe	92.083	0.38	92.526	0.33	Balance

4.4. Preliminary Printing Results

Composition 1 was used for the initial exploration of printing parameters for the bulk DMA AF96 feedstock. The DMA AF96 bulk feedstock visually exhibited smooth, free and consistent flowability. The consistency in powder flowability was expected as most of the powder particles from composition were spherical.

As seen in Table X (Appendix A), the irregular iron powder made up 32.6 grams of the mix composition. The remaining 67.4 grams of the composition were spherical. The irregular iron exhibited no clumpy particles.

Figure 25 shows the cubes printed from DMA AF96 powder with One Click MPRINT printer. Powder was fed from left to right of the build plate by the coater. Printing was successful for all cubes except for two cubes on the bottom right corner of the build plate, because of powder spreading dynamics and anomalies within the L-PBF machine. This happened because the build plate was tilted slightly to the left, and the powder in the bottom left corner was inadequate. Increasing the powder feed to the build plate solved the problem in phase 2 of the experiments.

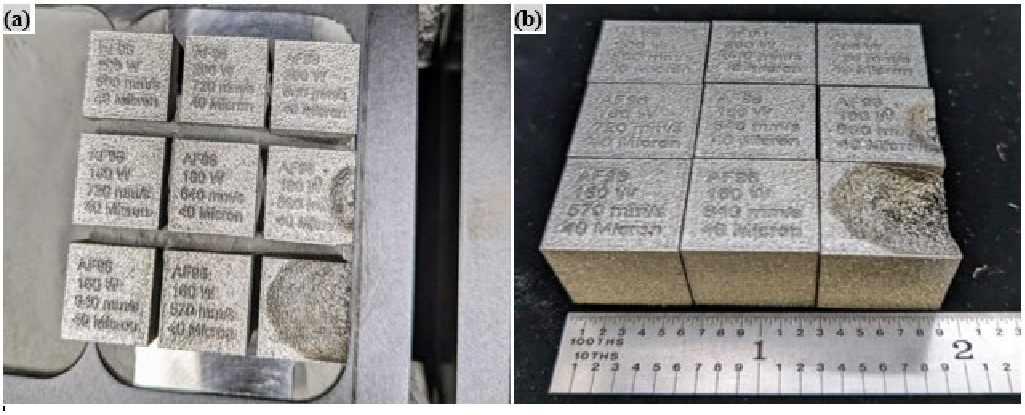

Figure 25: Printed Cubes of AF96 Deposits Showing Printing Defects

4.5. ARC Spark Spectrometry Analysis

Arc spark spectrometry was performed on all nine samples to confirm the composition weight percent. Three test runs were performed to serve as a consistency check in measuring the chemical composition of the deposits. Table VII compares the averages of the DMA AF96 test runs to the target composition of AF96 steel alloy.

As depicted in Table VII, all compositions were in the required specifications except for carbon and molybdenum. The composition for carbon in the deposits was slightly below the target composition by 0.002. This was attributed to the possibility of carbon vaporization during the L-PBF process. From Table X (Appendix A), the actual carbon weight percent from the DMA composition 1 was calculated at 0.243 wt.% which is not farther from the minimum target composition of 0.24 wt.% and the arc spark measured deposit composition of 0.238 wt.%.

The composition for molybdenum in the deposits was higher than the maximum target composition. It was later determined that the molybdenum composition (1.30 wt.%) for H13 powder on composition 1 (Table X , Appendix A) did not correspond to the actual composition (1.34 wt.%) on the data sheet from Carpenter additive manufacturing. This possibly caused the first composition of DMA AF96 to have high molybdenum content regions in the mix.

Table VII: Arc Spark Spectrometry Results of Phase 1 AF96 Deposits

AF96 Deposits Composition (wt.%)							
C	**Cr**	**Mn**	**V**	**Mo**	**Si**	**Ni**	**Fe**
0.238	2.468	0.492	0.217	1.579	0.456	1.984	92.300
AF96 Target Composition (wt.%)							
0.24-0.32	2.00-3.00	< 1	0.05-0.35	0.50-1.50	< 1.5	< 3	Balance

Further analyses were conducted to understand how the chemical compositions of carbon and molybdenum changed compared to the travel speeds and linear energy density during melting of the powder feedstock (Figure 26 and 27). Travel speeds for the left column cubes of the build plate were denoted as high travel speed, medium travel speed for the middle and low travel speed for right column cubes.

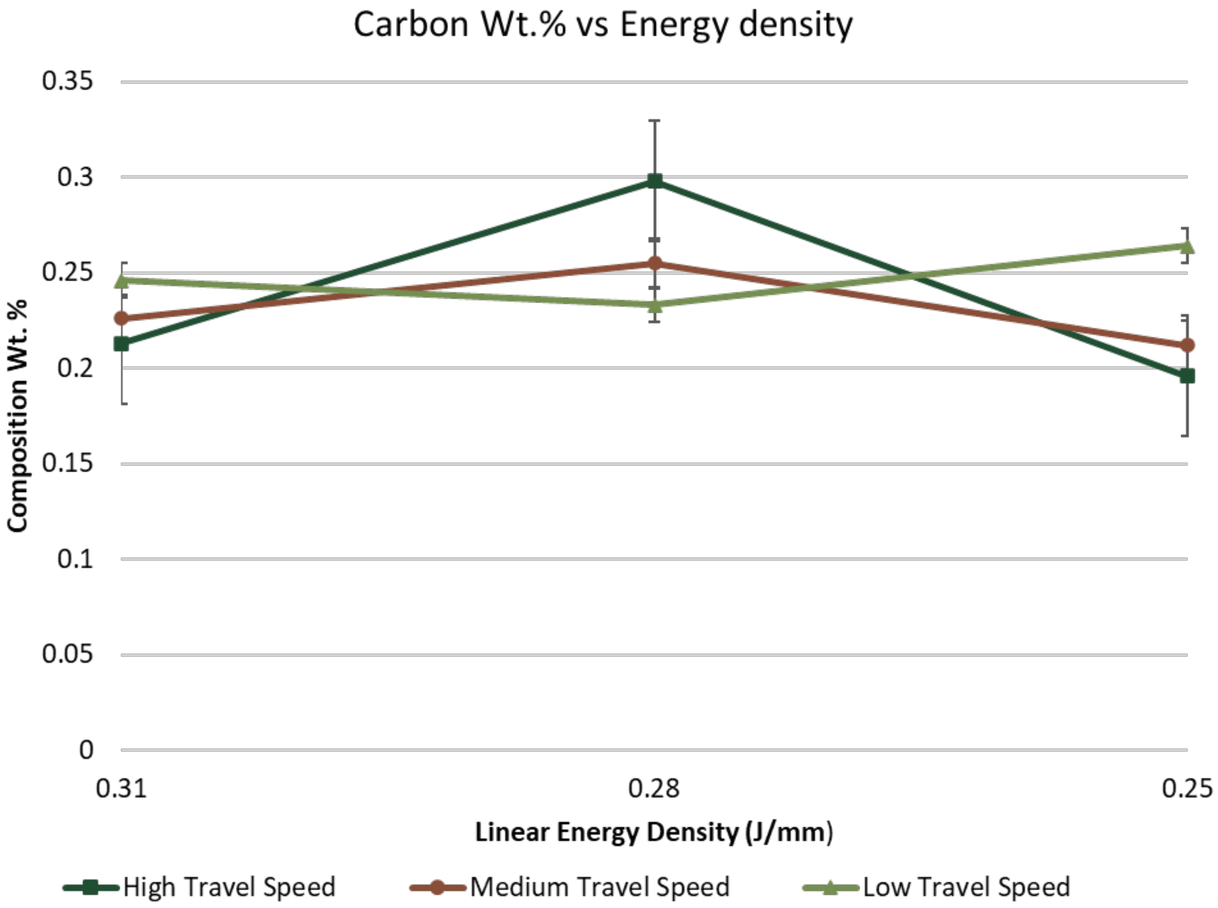

Figure 26: Arc Spark Analysis of Carbon Wt.% Vs. Energy Density

Results from Figure 26 show an unstable mixing of the carbon composition at higher travel speeds rising from 0.2 wt.% at the lowest linear energy density to 0.3 wt.% and reducing again to 0.21 wt.% at the highest energy density. A similar situation is seen at medium travel speeds. At low travel speeds the carbon composition seems stable with 0.25 wt.% at the highest energy density. Stability and uniform mixing during melting is mostly expected at low travel speeds.

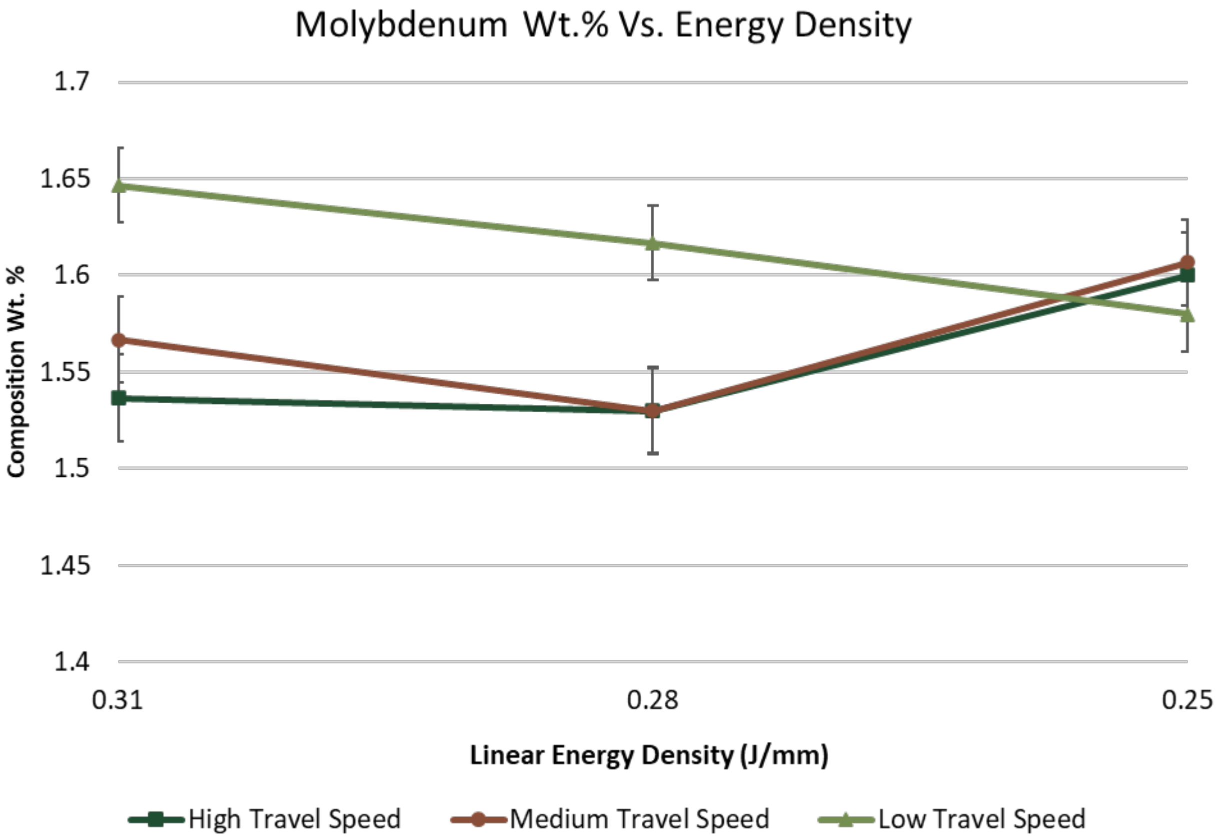

Figure 27: Arc Spark Analysis of Molybdenum Wt.% Vs. Energy Density

From Figure 27, molybdenum shows an unstable mixing and relation to the energy density during melting and powder mixing at higher and medium travel speeds. At low travel speed, it is observed that the composition weight percent increases steadily with increasing energy density. The weight percents in general are noticeably above 1.5 wt.% which is the max target composition for molybdenum in AF96 signifying a molybdenum rich composition.

4.6. SEM Analysis for Phase One

SEM micrographs for phase 1 printed deposits were taken to analyze the feedstock powder mixing during the melting and printing of the cubes. The melt pool characteristics (bright white strips) in the images of Figure 28 depict a heterogeneous composition of the DMA powder during melting. The white strips indicated that the DMA feedstock powder was rich in a specific chemical composition. Mixing improves with slow travel speeds at increased linear energy density across the build plate.

SEM-EDS spot analysis performed on the bright white strips in the images indicated that the DMA feedstock powder was rich in molybdenum (Mo was poorly mixed). The mixing homogeneity appears to improve at 160 W laser power with 570 mm/s and 520 mm/s travel speeds.

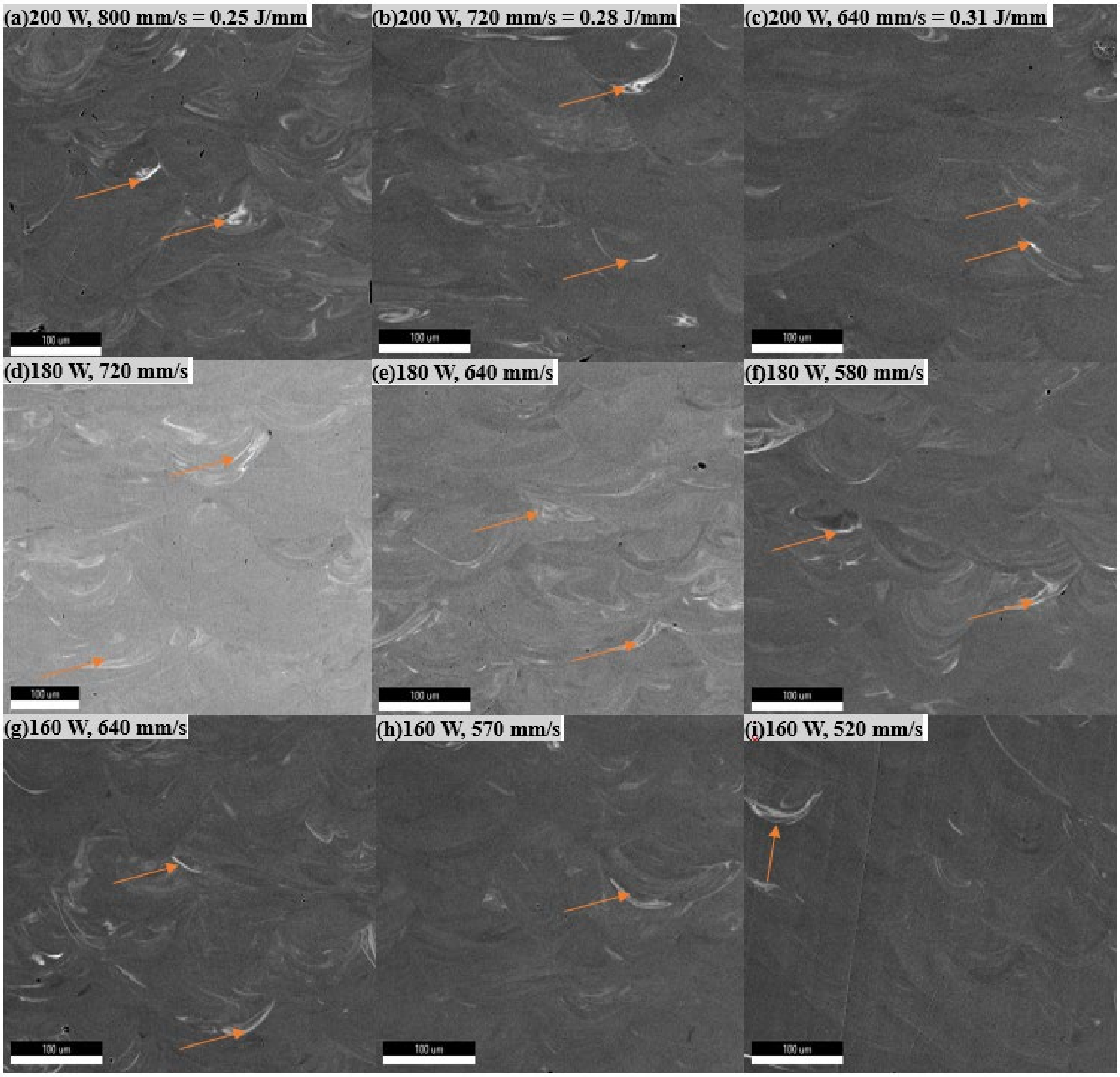

Figure 28: SEM Micrographs of the Printed Deposits with Increasing Linear Energy Density Showing Heterogeneous Composition. Arrows Pointing to Heterogeneous Regions

4.6.1. SEM Analyses for Phase Two

Figure 29 depicts an improved mixing and homogeneity of the AF96 deposits for phase two experiments. The linear energy densities were further increased across the build plate by reducing the travel speed. Comparing Figure 28 to 29, a noticeable fade of the bright white strips was observed indicating improved homogeneity from phase one to phase two and justifying the arc spark spectrometry results. A linear energy density to 0.5 J/mm at 160 W power, and 320 mm/s travel speed had the best results and may have been due to the DMA powder having enough time to mix while melting.

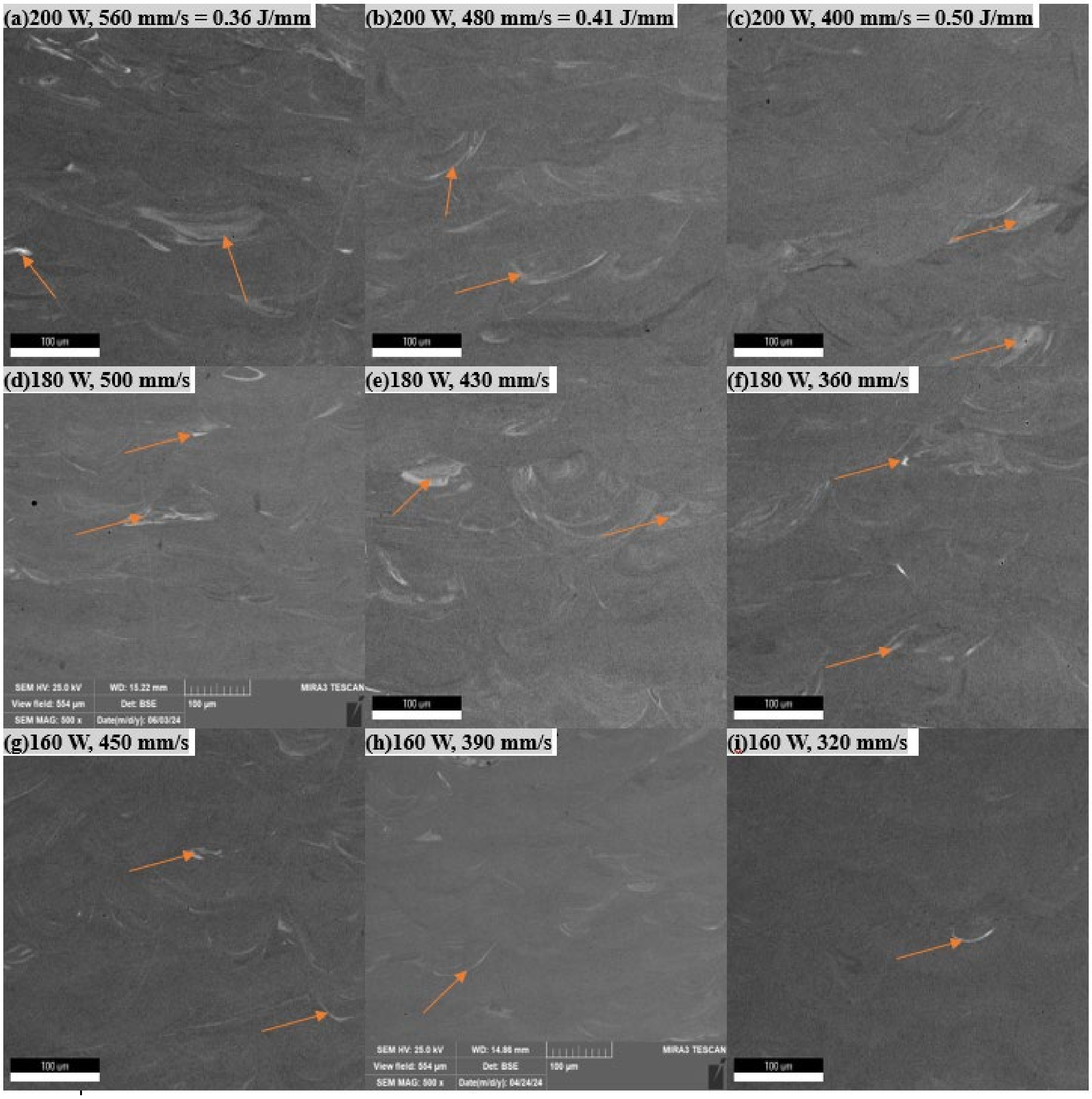

Figure 29: SEM Micrographs of Phase 2 Deposits Showing Improved Homogeneity. Arrows Pointing to Heterogenous Regions

4.6.2. Discontinuities and Void Formation in Melt Pool

The choice of powder characteristics is critical for optimizing the L-PBF process. Spherical powders with a size range of 15-45 um are generally preferred due to their superior flowability, packing density, and ability to produce high-quality printed parts with desirable mechanical properties [12]. Ensuring these powder characteristics can help in achieving consistent layer spreading, reduced porosity, and improved strength and durability of the final components.

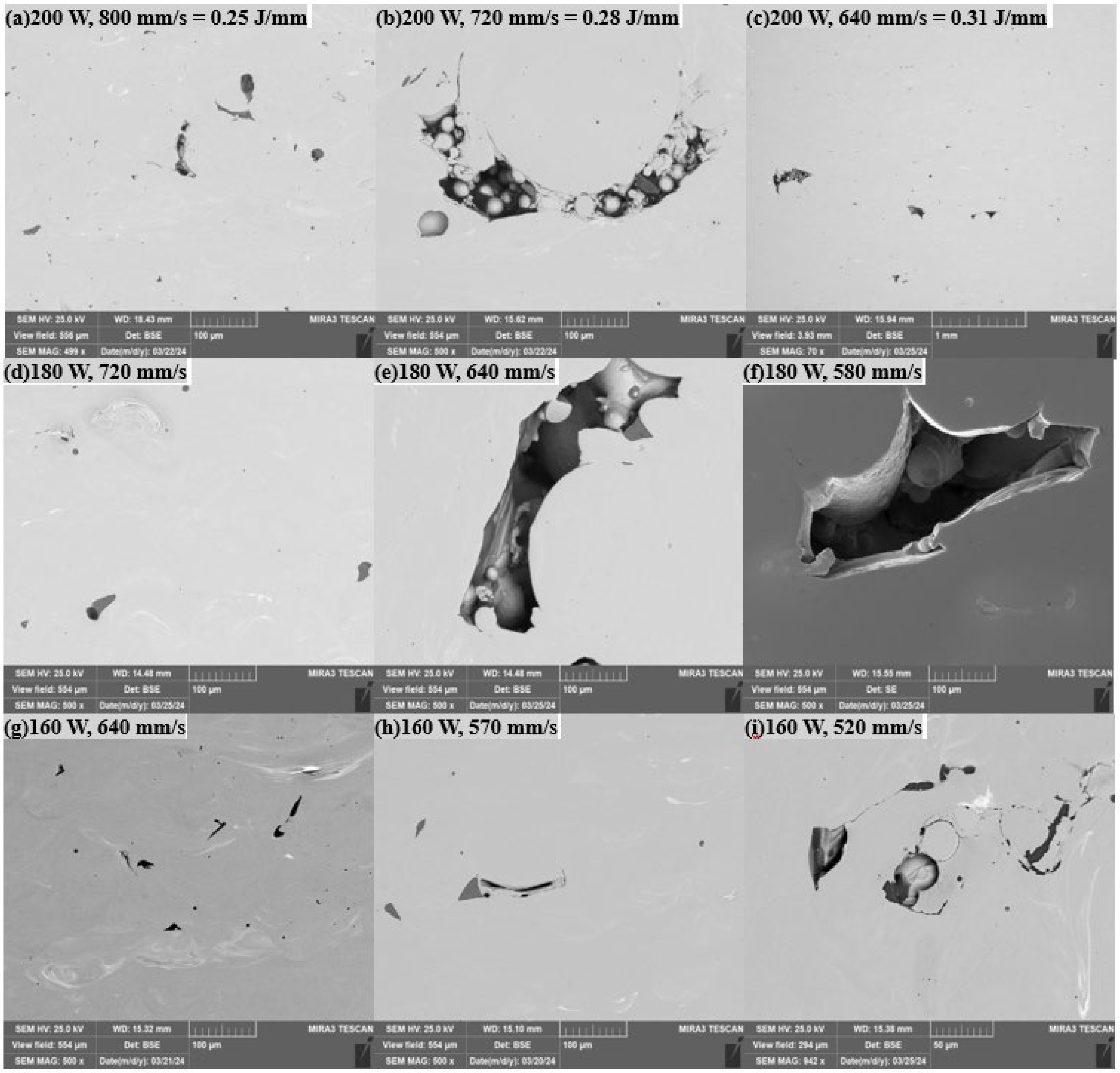

Figure 30: SEM Micrographs Showing Discontinuities in Phase 1 Deposits

Figure 30 noticeably shows defects like pore formation and presence of unmelted powder particles in phase one deposits. The larger particles in the 420 SS may have caused a sparse and discontinuous powder bed leading to the observed defects. Furthermore, it appears that the larger particles stuck to the previously scanned pool, as shown in Figure 30(b), 30(e), and 30(f), served as an obstacle and prevented the molten metal from filling the void.

The inhomogeneous powder distribution caused some places to be mounded resulting in incomplete powder melt. Fusion was unsteady and more discontinuous as less denser printing layers were formed. The larger powder may have contributed to low packing density resulting in internal voids.

The experimental results showed fewer discontinuities at higher energy densities and slow travel speeds, especially at 160 W laser power and 520 mm/s travel speed, indicating a more efficient laser-powder interaction. This can be attributed to a higher depth and width of pool at higher energy density (ED), which melted the remaining powder particle and filled up the void space remaining from the preceding scanning. At lower energy densities (i.e., higher laser power and faster travel speeds), the discontinuities and pore population appeared to be more rampant than at higher energy densities. The irregular iron powder may have also contributed to the increased porosity in the printed parts.

4.6.3. SEM Micrographs Showing Less Discontinuities

Wide field images were taken at 20 X magnification for phase two samples on the x-plane. Population of voids and discontinuities were noticed to have reduced remarkably at slower travel speeds and higher energy density than samples from phase one experiments. From Figure 31, the 160 W laser power shows the best results with almost no visible voids.

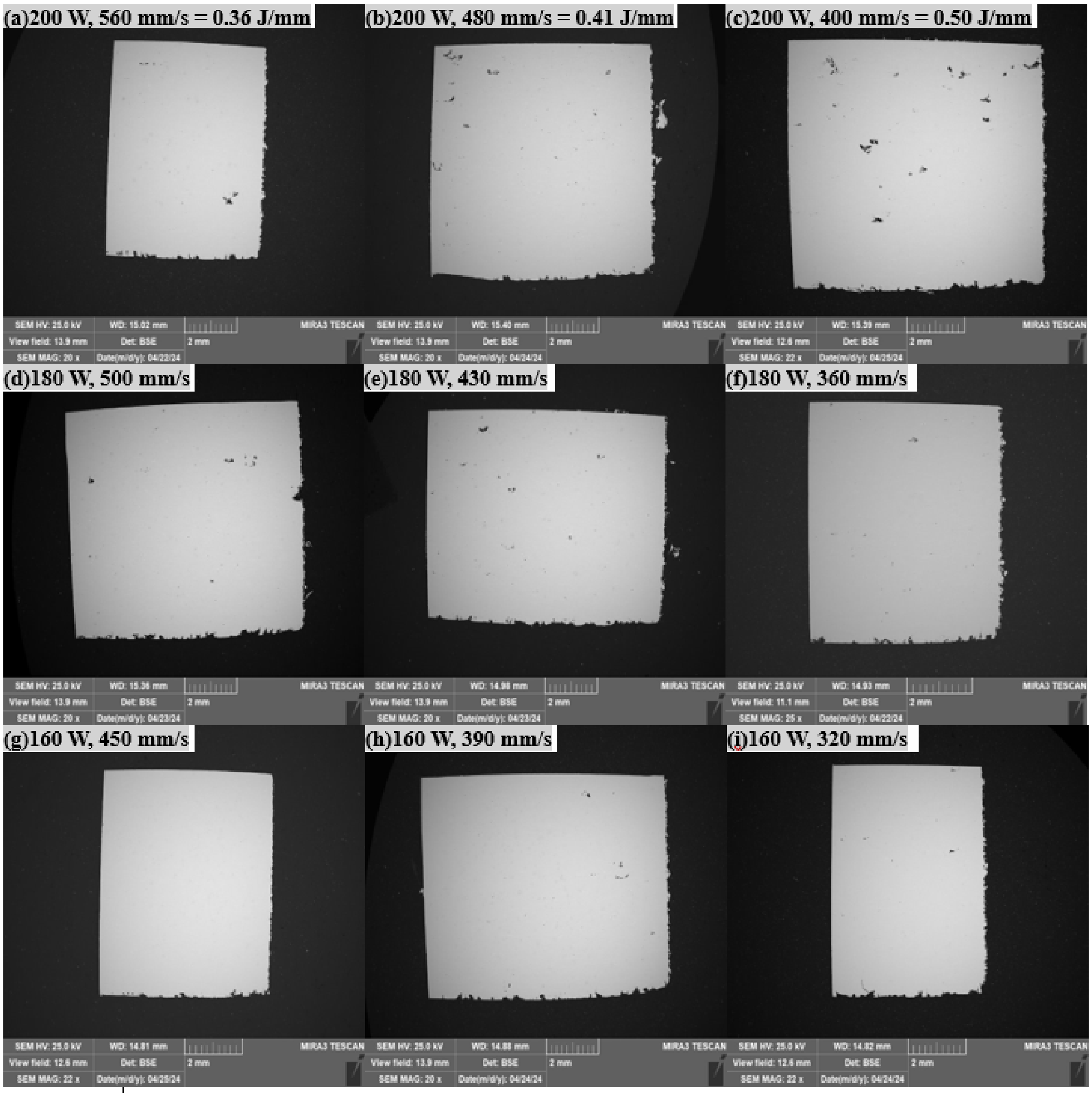

Figure 31: Wide Field SEM Micrographs Showing Less Discontinuities at Slower Travel Speeds

Flowability and packing density may have improved significantly given that the amount of irregular powder was reduced from 32.52 grams in composition one to 19.46 grams in composition two.

4.6.4. Arc Spark Spectrometry Analysis for Phase 2 Experiments

Table VIII shows the averages of the arc spark spectrometry data collected for the DMA deposits. The results showed an improvement in composition where carbon increased, and molybdenum decreased to the required target composition for AF96.

Table VIII: Arc Spark Spectrometry Results of Phase 2 AF96 deposits

AF96 Deposits Composition (wt.%)							
C	**Cr**	**Mn**	**V**	**Mo**	**Si**	**Ni**	**Fe**
0.254	2.283	0.459	0.183	1.367	0.498	2.326	92.340
AF96 Target Composition (wt.%)							
0.24-0.32	2.00-3.00	< 1	0.05-0.35	0.50-1.50	< 1.5	< 3	Balance

4.6.5. SEM-EDS Lines Scan Analysis

Figure 32 compares the relative standard deviation in elemental composition against the linear energy density for each constituent. Six line scans were taken on the sample's x-plane. The %RSD values were calculated by dividing the standard deviation of the line scan by its mean and then multiplying by 100%. The %RSD is a standardized approach to measure how precise the average of the line scans are compared to its mean. Low values of %RSD indicate an improved homogeneity within the DMA deposits and vice versa.

The travel speeds for the left column of the deposits on the build plate represent the high travel speed, the middle column represents the medium travel speed, and the right column represents the low travel speed. The %RSD values were plotted for phase 1 and 2 experiments in increasing order of the linear energy density.

A general trend of the %RSD improving with a higher energy density is noticed on the graphs. Again, the %RSD appears stable for all the alloying elements at medium and low travel speeds except for nickel. The high %RSD of carbon, vanadium, and manganese respectively were expected to be unstable because of their small quantity in the AF96 composition compared to the other elements. Although the %RSD improved for the second phase of experiments, the results quantify a lack of homogeneity present within the DMA deposits.

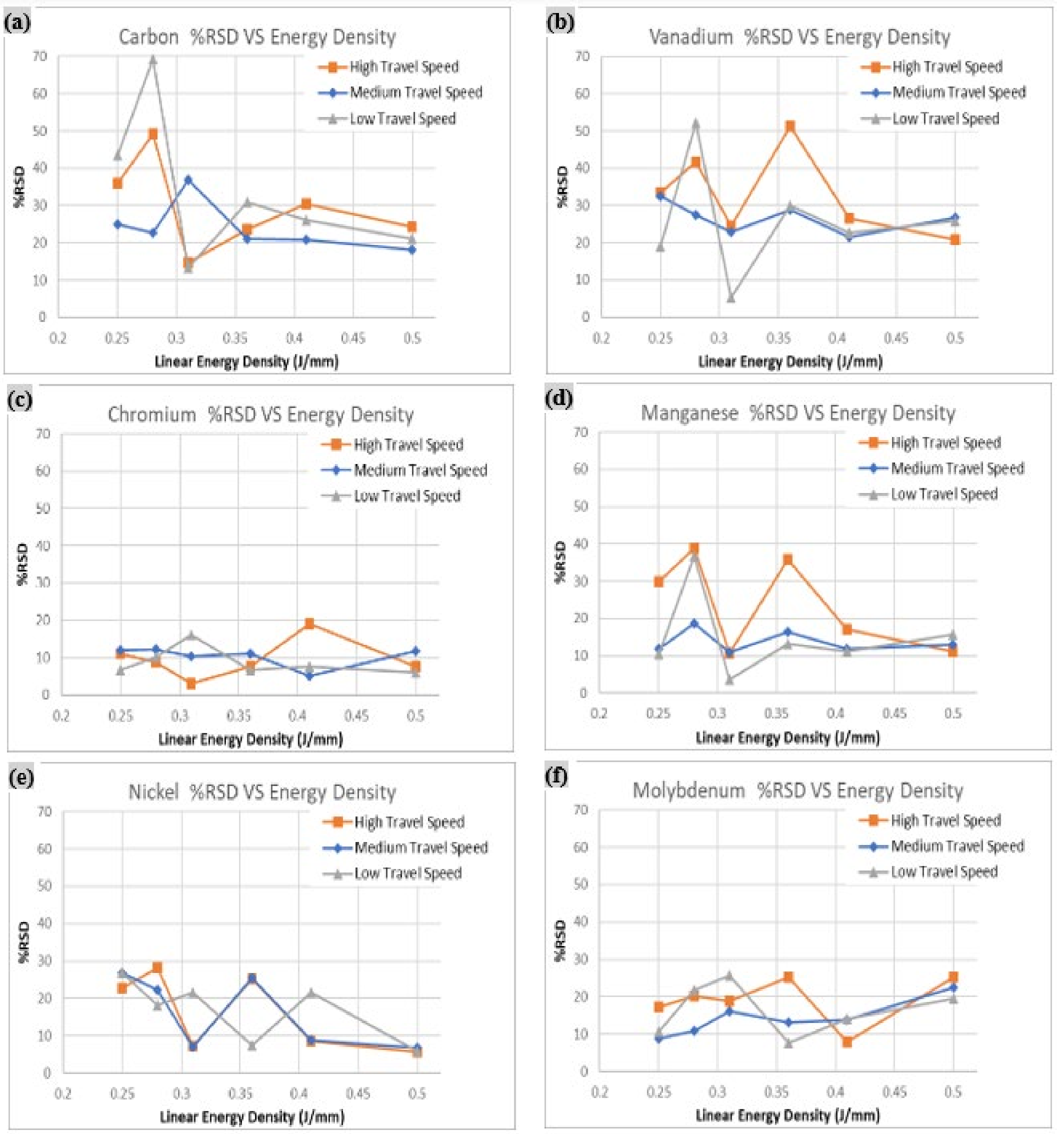

Figure 32: AF96 Constituent %RSD Vs. Energy Density

4.6.6. Comparison of %RSD of DMA AF96 Deposits to Industrially Cast Alloy

AF96 alloy is amenable to casting and forging. To justify the DMA AF96 results, the %RSD results of an industrial cast alloy with a similar composition were used as a benchmark to compare the line scan results. The %RSD results were calculated from 12 line scans performed on the industrially cast alloy, six line scans each at two different areas of the sample. The results were compared to the %RSD results (for all nine samples) of the phase two DMA deposits (Table IX).

Most of the %RSD results for the DMA AF96 deposits were better than the %RSD results of the industrial cast alloy. The %RSD results of the DMA deposits were consistent with the %RSD results of the industrially cast Fe-Ni-Mo-Mn-Cr-V-Si-C alloy.

Table IX: %RSD Values for DMA Deposits and Industrial Cast Alloy

Element	%RSD AF96 DMA Deposits	%RSD Industrially Cast Alloy
C	24.043	16.278
Si	30.104	30.425
V	28.241	59.379
Cr	9.108	11.449
Mn	16.183	15.818
Fe	0.994	0.880
Ni	12.820	18.319
Mo	16.571	17.602

4.7. Rockwell Hardness Test Results

The hardness test results were compared to the linear energy densities of samples from phase one and two. A higher hardness result was noticed (Figure 33) at a linear energy density of 0.25 J/mm. Meanwhile, hardness is seen to decrease for higher linear energy densities of 0.31 J /mm and 0.5 J/mm.

The hardness change may be due to the varying travels speeds from phase one to two. Higher travel speeds result in lower heat input (linear energy density). This leads to faster cooling rates and may increase the hardness of the deposit. Faster cooling can form harder microstructures, like martensite in steels. In contrast, lower travel speed results in higher heat input, which allows more time for grain growth and can result in softer microstructures due to slower cooling rates. Although the varying travel speeds may affect the changes in hardness, there is no certainty as other factors beyond our control, like laser absorptivity and powder vaporization, may be at play during deposition.

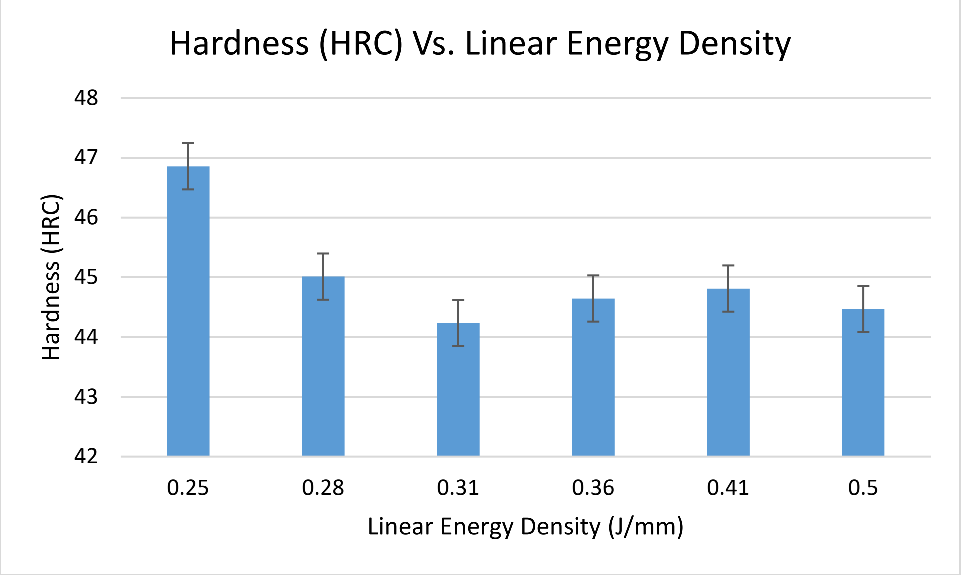

Figure 33: Relationship between Hardness and Linear Energy Density

5. Conclusion

The following conclusions were drawn after results from the experiments.

Mixing of AF96 powder feedstock using Dry Metal Alloying was successful. Although homogeneity improved from phase one to phase two, the DMA AF96 deposits exhibited inhomogeneous composition. Overall, the DMA deposits at 160 W power showed the best results from the tests performed.

The DMA AF96 powder feedstock was successfully used to print metal cubes on the One Click MPRINT printer and SEM micrographs, EDS line scans and arc spark spectrometry were used to determine the homogeneity of the deposits.

DMA AF96 deposits showed consistent % RSD results to the industrially cast Fe-Ni-Mo-Mn-Cr-V-Si-C alloy.

From the SEM micrographs, it was observed that most powder particles melted well, but due to a nonuniform powder distribution, some portions were mounded and did not melt completely. Slower travel speeds showed better mixing and homogeneity with reduced population of discontinuities especially at 160 W laser power.

The Rockwell hardness test results indicated hardness increasing with decreasing linear energy density.

6. Recommendation

6.1. DMA Powder Composition

The enhancement of powder characteristics is one of the ways to improve the production of AM parts with improved surface quality and mechanical properties. The irregular iron powder should be changed to spherical powder as it might affect packing density and improve the homogeneity of the DMA powder and deposits.

The 420 SS should be re-sieved to take out the larger powder particles and packing density should be measured for comparison.

6.2. L-PBF Deposits

Continue with slower travel speeds especially for 160 W laser power. Higher power could also be explored for slower travel speeds.

Oscillate the laser in different pattern to solve heterogeneity issue which in turn curbs the discontinuities.

Microstructural analyses should be performed on the deposits to know the phases present and understand the phases that affects the mechanical properties of the DMA AF96 alloy.

7. References Cited

1. Sames, W. J., List, F. A., Pannala, S., Dehoff, R. R., & Babu, S. S. (2016). The metallurgy and processing science of metal additive manufacturing. *International materials reviews*, *61*(5), 315-360.
2. Smoqi, Z., Gaikwad, A., Bevans, B., Kobir, M. H., Craig, J., Abul-Haj, A., ... & Rao, P. (2022). Monitoring and prediction of porosity in laser powder bed fusion using physics-informed meltpool signatures and machine learning. *Journal of Materials Processing Technology*, *304*, 117550.
3. Imani, F., Gaikwad, A., Montazeri, M., Rao, P., Yang, H., & Reutzel, E. (2018). Process mapping and in-process monitoring of porosity in laser powder bed fusion using layerwise optical imaging. *Journal of Manufacturing Science and Engineering*, *140*(10), 101009.
4. Grasso, M., & Colosimo, B. M. (2017). Process defects and in situ monitoring methods in metal powder bed fusion: a review. *Measurement Science and Technology*, *28*(4), 044005.
5. Gaikwad, A., Williams, R. J., de Winton, H., Bevans, B. D., Smoqi, Z., Rao, P., & Hooper, P. A. (2022). Multi phenomena melt pool sensor data fusion for enhanced process monitoring of laser powder bed fusion additive manufacturing. *Materials & Design*, *221*, 110919.
6. Yavari, R., Riensche, A., Tekerek, E., Jacquemetton, L., Halliday, H., Vandever, M., ... & Rao, P. (2021). Digitally twinned additive manufacturing: Detecting flaws in laser powder bed fusion by combining thermal simulations with in-situ meltpool sensor data. *Materials & Design*, *211*, 110167.

7. Yang, H., Rao, P., Simpson, T., Lu, Y., Witherell, P., Nassar, A. R., ... & Kumara, S. (2020). Six-sigma quality management of additive manufacturing. *Proceedings of the IEEE*, *109*(4), 347-376.
8. Mani, M., Feng, S., Brandon, L., Donmez, A., Moylan, S., & Fesperman, R. (2017). Measurement science needs for real-time control of additive manufacturing powder-bed fusion processes. In *Additive manufacturing handbook* (pp. 629-652). CRC Press.
9. Sow, M. C., De Terris, T., Castelnau, O., Hamouche, Z., Coste, F., Fabbro, R., & Peyre, P. (2020). Influence of beam diameter on Laser Powder Bed Fusion (L-PBF) process. *Additive Manufacturing*, *36*, 101532.
10. Lu, X. (2022). Computational and experimental thermo-mechanics of metal additive manufacturing: stress, warpage, cracks, and properties.
11. Liu, J., & Wen, P. (2022). Metal vaporization and its influence during laser powder bed fusion process. *Materials & Design*, *215*, 110505.
12. Mostafaei, A., Zhao, C., He, Y., Ghiaasiaan, S. R., Shi, B., Shao, S., ... & Rollett, A. D. (2022). Defects and anomalies in powder bed fusion metal additive manufacturing. *Current Opinion in Solid State and Materials Science*, *26*(2), 100974.
13. Gibbons, D. W., Govender, P., & van der Merwe, A. F. (2023). Metal powder feedstock evaluation and management for powder bed fusion: a review of literature, standards, and practical guidelines. *Progress in Additive Manufacturing*, 1-29.
14. Shah, D. S., Moravkar, K. K., Jha, D. K., Lonkar, V., Amin, P. D., & Chalikwar, S. S. (2023). A concise summary of powder processing methodologies for flow enhancement. *Heliyon*.

15. Shah, U. V., Karde, V., Ghoroi, C., & Heng, J. Y. (2017). Influence of particle properties on powder bulk behaviour and processability. *International journal of pharmaceutics*, *518*(1-2), 138-154.
16. Hanson, S., Vadiraja, S., and Huft, N., 2024, Compositional and Microstructural characterization of 304L and 316L Stainless Steels Produced by L-PBF Additive Manufacturing Using Novel Dry Metal Alloy (DMA) Powder Feedstock: TMS 2024 Annual Meeting & Exhibition, March 5, 2024, Orlando, FL.
17. Mosallanejad, M. H., Niroumand, B., Aversa, A., & Saboori, A. (2021). In-situ alloying in laser-based additive manufacturing processes: A critical review. *Journal of Alloys and Compounds*, *872*, 159567.
18. Knieps, M. S., Reynolds, W. J., Dejaune, J., Clare, A. T., & Evirgen, A. (2021). In-situ alloying in powder bed fusion: The role of powder morphology. *Materials Science and Engineering: A*, *807*, 140849.
19. Kumar, R., Kumar, M., & Chohan, J. S. (2021). The role of additive manufacturing for biomedical applications: A critical review. *Journal of Manufacturing Processes*, *64*, 828-850.
20. Wischeropp, T. M. (2021). Advancement of Selective Laser Melting by Laser Beam Shaping. Germany: Springer, Imprint: Springer Vieweg.pg. 7.
21. Mechanical Jungle. (2022). *What is forming, types of forming, forming processes in manufacturing and metal forming processes.* https://mechanicaljungle.com/forming/
22. Frazier, W. E. (2014). Metal additive manufacturing: a review. *Journal of Materials Engineering and performance*, *23*, 1917-1928.

23. Beaman, J. J., Bourell, D. L., Seepersad, C. C., & Kovar, D. (2020). Additive manufacturing review: Early past to current practice. Journal of Manufacturing Science and Engineering, 142(11).
24. Li, M., Du, W., Elwany, A., Pei, Z., & Ma, C. (2020). Metal binder jetting additive manufacturing: a literature review. Journal of Manufacturing Science and Engineering, 142(9).
25. Attaran, M. (2017). The rise of 3-D printing: The advantages of additive manufacturing over traditional manufacturing. Business horizons, 60(5), 677-688.
26. Grand View Research. (2024). *Additive Manufacturing Market Size, Share & Trends Analysis Report, By Component, By Printer Type, By Technology, By Software, By Application, By Vertical, By Material, By Region, And Segment Forecasts, 2024 – 2030.* https://www.grandviewresearch.com/industry-analysis/additive-manufacturing-market.
27. Yadroitsev, I., Yadroitsava, I., Du Plessis, A., & MacDonald, E. (Eds.). (2021). Fundamentals of laser powder bed fusion of metals. Elsevier.
28. DeBoer, B., Nguyen, N., Diba, F. et al. Additive, subtractive, and formative manufacturing of metal components: a life cycle assessment comparison. Int J Adv Manuf Technol 115, 413–432 (2021). https://doi.org/10.1007/s00170-021-07173-5.
29. Ziaee, M., & Crane, N. B. (2019). Binder jetting: A review of process, materials, and methods. Additive Manufacturing, 28, 781-801.
30. Mostafaei, A., Elliott, A. M., Barnes, J. E., Li, F., Tan, W., Cramer, C. L., ... & Chmielus, M. (2021). Binder jet 3D printing—Process parameters, materials, properties, modeling, and challenges. Progress in Materials Science, 119, 100707.

31. Sefene, E. M. (2022). State-of-the-art of selective laser melting process: A comprehensive review. Journal of Manufacturing Systems, 63, 250-274.
32. Pereira, T., Kennedy, J. V., & Potgieter, J. (2019). A comparison of traditional manufacturing vs additive manufacturing, the best method for the job. Procedia Manufacturing, 30, 11-18.
33. Huang, S. H., Liu, P., Mokasdar, A., & Hou, L. (2013). Additive manufacturing and its societal impact: a literature review. The International journal of advanced manufacturing technology, 67, 1191-1203.
34. Singh, D. D., Mahender, T., & Reddy, A. R. (2021). Powder bed fusion process: A brief review. Materials Today: Proceedings, 46, 350-355.
35. Guo, N., & Leu, M. C. (2013). Additive manufacturing: technology, applications, and research needs. Frontiers of mechanical engineering, 8, 215-243.
36. Jorge, J. C. F., De Souza, L. F. G., Mendes, M. C., Bott, I. S., Araújo, L. S., Dos Santos, V. R., ... & Evans, G. M. (2021). Microstructure characterization and its relationship with impact toughness of C–Mn and high strength low alloy steel weld metals–a review. *Journal of Materials research and technology*, *10*, 471-501.
37. Sangeetha, N., Monish, P., & Brathikan, V. M. (2022, March). Review on various materials used in Additive Manufacturing. In *IOP Conference Series: Materials Science and Engineering* (Vol. 1228, No. 1, p. 012015). IOP Publishing.
38. Ngo, T. D., Kashani, A., Imbalzano, G., Nguyen, K. T., & Hui, D. (2018). Additive manufacturing (3D printing): A review of materials, methods, applications and challenges. *Composites Part B: Engineering*, *143*, 172-196.

39. King, W. E., Anderson, A. T., Ferencz, R. M., Hodge, N. E., Kamath, C., Khairallah, S. A., & Rubenchik, A. M. (2015). Laser powder bed fusion additive manufacturing of metals; physics, computational, and materials challenges. Applied Physics Reviews, 2(4).
40. Vock, S., Klöden, B., Kirchner, A., Weißgärber, T., & Kieback, B. (2019). Powders for powder bed fusion: a review. Progress in Additive Manufacturing, 4, 383-397.
41. Bhavar, V., Kattire, P., Patil, V., Khot, S., Gujar, K., & Singh, R. (2017). A review on powder bed fusion technology of metal additive manufacturing. Additive manufacturing handbook, 251-253.
42. DebRoy, T., Wei, H. L., Zuback, J. S., Mukherjee, T., Elmer, J. W., Milewski, J. O., ... & Zhang, W. (2018). Additive manufacturing of metallic components–process, structure, and properties. Progress in Materials Science, 92, 112-224.
43. Santecchia, E., Spigarelli, S., & Cabibbo, M. (2020). Material reuse in laser powder bed fusion: Side effects of the laser—metal powder interaction. Metals, 10(3), 341.
44. Buhairi, M. A., Foudzi, F. M., Jamhari, F. I., Sulong, A. B., Radzuan, N. A. M., Muhamad, N., ... & Al-Furjan, M. S. H. (2023). Review on volumetric energy density: influence on morphology and mechanical properties of Ti6Al4V manufactured via laser powder bed fusion. Progress in Additive Manufacturing, 8(2), 265-283.
45. Peng, T., & Chen, C. (2018). Influence of energy density on energy demand and porosity of 316L stainless steel fabricated by selective laser melting. International Journal of Precision Engineering and Manufacturing-Green Technology, 5, 55-62.
46. Sow, M. C., De Terris, T., Castelnau, O., Hamouche, Z., Coste, F., Fabbro, R., & Peyre, P. (2020). Influence of beam diameter on Laser Powder Bed Fusion (L-PBF) process. Additive Manufacturing, 36, 101532.

47. Mukherjee, T., Manvatkar, V., De, A., & DebRoy, T. (2017). Mitigation of thermal distortion during additive manufacturing. *Scripta materialia*, *127*, 79-83.
48. Xie, D., Lv, F., Yang, Y., Shen, L., Tian, Z., Shuai, C., ... & Zhao, J. (2022). A review on distortion and residual stress in additive manufacturing. Chinese Journal of Mechanical Engineering: Additive Manufacturing Frontiers, 1(3), 100039.
49. Abrahams, R. (Dec.22, 2016), *Low Alloy High Performance Steel*, US 2016/0369362 A1, United States.
50. Kassym, K., & Perveen, A. (2020). Atomization processes of metal powders for 3D printing. Materials today: proceedings, 26, 1727-1733.
51. Upadhyaya, G. S. (1997). *Powder metallurgy technology*. Cambridge Int Science Publishing.
52. Asgarian, A., Wu, C., Li, D., Bussmann, M., Chattopadhyay, K., Lemieux, S., ... & Paserin, V. (2018). Experimental and computational analysis of a water spray; application to molten metal atomization. In *Advances in powder metallurgy and particulate materials (Proceedings of the 2018 International Conference on Powder Metallurgy & Particulate Materials)* (pp. 126-137).
53. R. E. Schafrik, "Manufacture of TiAl by extrusion of blended elemental powders," *Metall.Trans. B*, vol. 7, no. 4, pp. 713–716, 1976, doi: 10.1007/BF02698608.
54. S. Ewald, F. Kies, S. Hermsen, M. Voshage, C. Haase, and J. H. Schleifenbaum, "Rapid alloy development of extremely high-alloyed metals using powder blends in laser powder bed fusion," *Materials (Basel).*, vol. 12, no. 10, 2019, doi: 10.3390/MA12101706.
55. S. Karnati, "Characterization of copper – nickel alloys fabricated using laser metal deposition and blended powder feedstocks," pp. 239–250, 2019.

56. J. G. Osorio and F. J. Muzzio, “Evaluation of resonant acoustic mixing performance, ”*Powder Technol.*, vol. 278, pp. 46–56, 2015, doi: 10.1016/j.powtec.2015.02.033.
57. W. Li, L. Yan, X. Chen, J. Zhang, X. Zhang, and F. Liou, “Directed energy depositing a new Fe-Cr-Ni alloy with gradually changing composition with elemental powder mixes and particle size’ effect in fabrication process,” *J. Mater. Process. Technol.*, vol. 255, no. December 2017, pp. 96–104, 2018, doi: 10.1016/j.jmatprotec.2017.12.010.
58. T. Takeda, W. M. Steen, and D. R. F. West, “Laser Cladding With Mixed Powder Feed.,”*LIA (Laser Inst. Am.*, vol. 43, no. 1984, pp. 151–158, 1985, doi: 10.2351/1.5057597.
59. R. Zhao, J. Gao, H. Liao, N. Fenineche, and C. Coddet, “Selective laser melting of elemental powder blends for fabrication of homogeneous bulk material of near-eutectic Ni–Sn composition,” *Addit. Manuf.*, vol. 34, no. March, p. 101261, 2020, doi:10.1016/j.addma.2020.101261.
60. T. O. W. R.L. McNabb, P.A. Lucon, N.J. Huft, “Dry Metal Alloying Compositions and Related Methods,” US Provisonal Patent Filing Application Numbers: 63119420,3064758.
61. Babu, S. S., David, S. A., & Vitek, J. M. (1995). *Phase transformations and microstructure development in low alloy steel welds* (No. CONF-9508134-1). Oak Ridge National Lab.(ORNL), Oak Ridge, TN (United States).
62. Grong, O., & Matlock, D. K. (1986). Microstructural development in mild and low-alloy steel weld metals. *International metals reviews*, *31*(1), 27-48.
63. Muñiz-Lerma, J. A., Nommeots-Nomm, A., Waters, K. E., & Brochu, M. (2018). A comprehensive approach to powder feedstock characterization for powder bed fusion additive manufacturing: a case study on AlSi7Mg. *Materials*, *11*(12), 2386.

64. Brika, S. E., Letenneur, M., Dion, C. A., & Brailovski, V. (2020). Influence of particle morphology and size distribution on the powder flowability and laser powder bed fusion manufacturability of Ti-6Al-4V alloy. *Additive Manufacturing*, *31*, 100929.

65. Mathias, L. E., Pinotti, V. E., Batistão, B. F., Rojas-Arias, N., Figueira, G., Andreoli, A. F., & Gargarella, P. (2024). Metal powder as feedstock for laser-based additive manufacturing: From production to powder modification. *Journal of Materials Research*, *39*(1), 19-47.

66. Stegman, B. T., Lopez, J., Jarosinski, W., Wang, H., & Zhang, X. (2023). The Influence of Powder Particle Size Distributions on Mechanical Properties of Alloy 718 by Laser Powder Bed Fusion. *Metals*, *13*(8), 1384.

67. Spurek, M. A., Haferkamp, L., Weiss, C., Spierings, A. B., Schleifenbaum, J. H., & Wegener, K. (2021). Influence of the particle size distribution of monomodal 316L powder on its flowability and processability in powder bed fusion. *Progress in Additive Manufacturing*, 1-10.

68. Whiting, J. G., Tondare, V. N., Scott, J. H. J., Phan, T. Q., & Donmez, M. A. (2019). Uncertainty of particle size measurements using dynamic image analysis. *CIRP Annals*, *68*(1), 531-534.

69. Cai, C., & Zhou, K. (2022). Metal additive manufacturing. *Digital Manufacturing*, 247-298.

70. Riener, K., Albrecht, N., Ziegelmeier, S., Ramakrishnan, R., Haferkamp, L., Spierings, A. B., & Leichtfried, G. J. (2020). Influence of particle size distribution and morphology on the properties of the powder feedstock as well as of AlSi10Mg parts produced by laser powder bed fusion (LPBF). *Additive Manufacturing*, *34*, 101286.

71. Hager, E. M. (2019). Process Parameter Development of Additively Manufactured AF9628 Weapons Steel.

8. Appendix A

Table X: Composition Calculator for Composition One

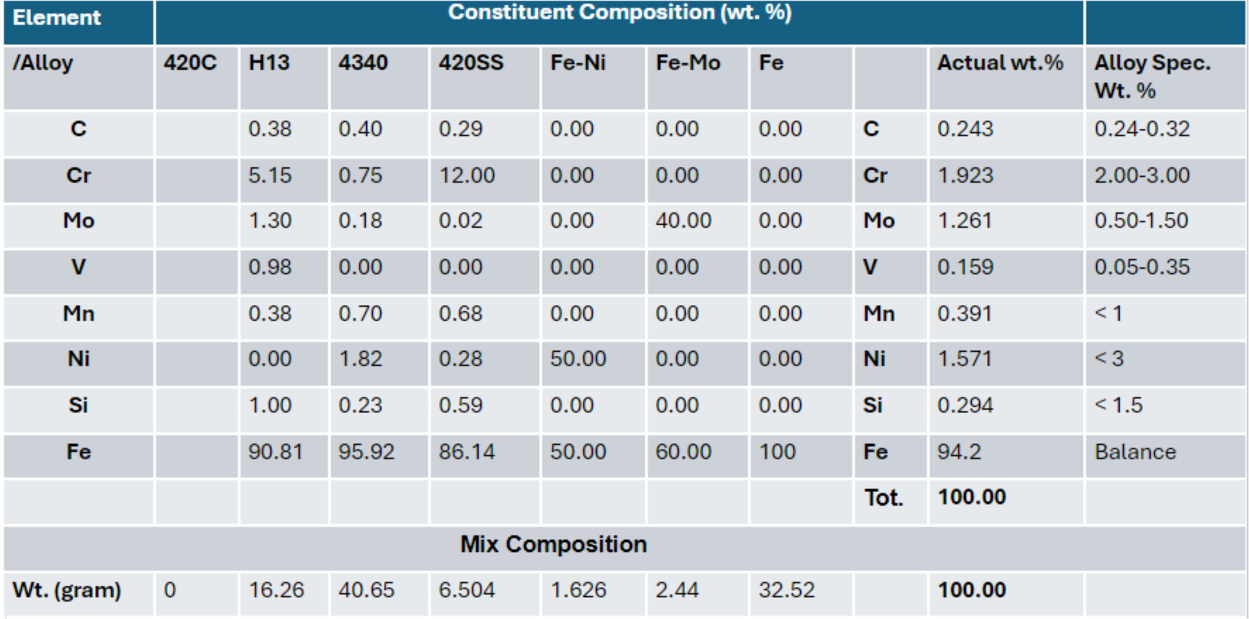

Element	**Constituent Composition (wt. %)**									
/Alloy	**420C**	**H13**	**4340**	**420SS**	**Fe-Ni**	**Fe-Mo**	**Fe**		**Actual wt.%**	**Alloy Spec. Wt. %**
C		0.38	0.40	0.29	0.00	0.00	0.00	**C**	0.243	0.24-0.32
Cr		5.15	0.75	12.00	0.00	0.00	0.00	**Cr**	1.923	2.00-3.00
Mo		1.30	0.18	0.02	0.00	40.00	0.00	**Mo**	1.261	0.50-1.50
V		0.98	0.00	0.00	0.00	0.00	0.00	**V**	0.159	0.05-0.35
Mn		0.38	0.70	0.68	0.00	0.00	0.00	**Mn**	0.391	< 1
Ni		0.00	1.82	0.28	50.00	0.00	0.00	**Ni**	1.571	< 3
Si		1.00	0.23	0.59	0.00	0.00	0.00	**Si**	0.294	< 1.5
Fe		90.81	95.92	86.14	50.00	60.00	100	**Fe**	94.2	Balance
								Tot.	**100.00**	
Mix Composition										
Wt. (gram)	0	16.26	40.65	6.504	1.626	2.44	32.52		**100.00**	

Table XI: Composition Calculator for Composition Two

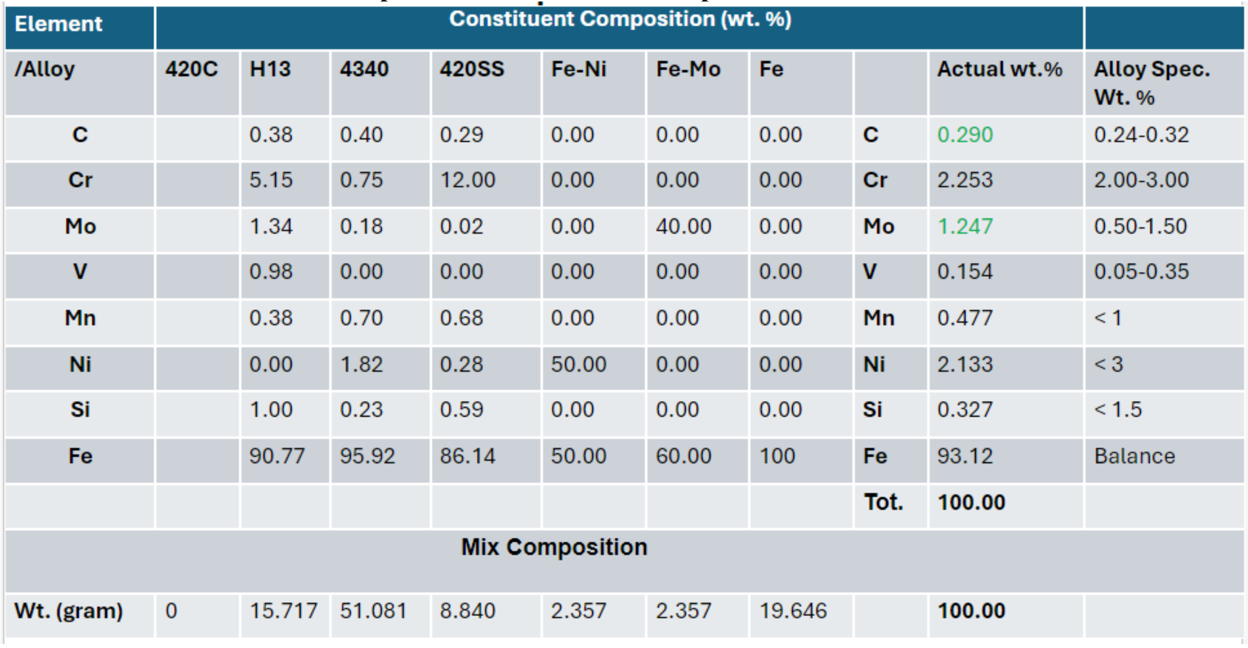

Element	**Constituent Composition (wt. %)**									
/Alloy	**420C**	**H13**	**4340**	**420SS**	**Fe-Ni**	**Fe-Mo**	**Fe**		**Actual wt.%**	**Alloy Spec. Wt. %**
C		0.38	0.40	0.29	0.00	0.00	0.00	**C**	0.290	0.24-0.32
Cr		5.15	0.75	12.00	0.00	0.00	0.00	**Cr**	2.253	2.00-3.00
Mo		1.34	0.18	0.02	0.00	40.00	0.00	**Mo**	1.247	0.50-1.50
V		0.98	0.00	0.00	0.00	0.00	0.00	**V**	0.154	0.05-0.35
Mn		0.38	0.70	0.68	0.00	0.00	0.00	**Mn**	0.477	< 1
Ni		0.00	1.82	0.28	50.00	0.00	0.00	**Ni**	2.133	< 3
Si		1.00	0.23	0.59	0.00	0.00	0.00	**Si**	0.327	< 1.5
Fe		90.77	95.92	86.14	50.00	60.00	100	**Fe**	93.12	Balance
								Tot.	**100.00**	
Mix Composition										
Wt. (gram)	0	15.717	51.081	8.840	2.357	2.357	19.646		**100.00**	